~~Scale-dependency of extreme heavy precipitation processes in regional climate simulations of the greater Alpine region~~ Regional Climate and Convection-Permitting Modelling of heavy precipitaiton in decadal simulations of the greater Alpine region with COSMO-CLM

Alberto Caldas-Alvarez[1], Hendrik Feldmann[1], Etor Lucio-Eceiza[2,3], and Joaquim G. Pinto[1]

[1]Institute of Meteorology and Climate Research (IMK-TRO), Karlsruhe Institute of Technology (KIT), Karlsruhe, 76131, Germany.

[2]Institute of Meteorology, Freie Universität Berlin (FUB), Berlin, 14195, Germany.

[3]Deutsches Klimarechenzentrum (DKRZ, German Climate Computing Center), Hamburg, 20146, Germany.

Correspondence to: Alberto Caldas-Alvarez (alberto.caldas-alvarez@kit.edu)

Abstract. Heavy Precipitation Events (HPEs) are a challenging atmospheric phenomenon with a high impact on human lives and infrastructures. The achievement of high-resolution simulations for Convection Permitting Modelling (CPM; $\Delta x < 4km$) has brought relevant advancements in the representation of HPEs. ~~in climate simulations compared to coarser resolution Regional Climate Models (RCM).~~ However, further insight is needed as to differences exist between Regional Climate Modelling (RCM) and CPM ~~on the scale-dependency of mesoscale precipitation processes.~~ In this study, we ~~aim~~ evaluate ~~at evaluating~~ reanalysis-driven climate simulations of the greater Alpine area in the period 2000-2015 and assess the differences in representing heavy precipitation and associated processes in a RCM and a CPM setup with the COSMO-CLM model. ~~in recent climate conditions and assessing the scale dependency of thermodynamical processes influencing extreme heavy precipitation. We evaluate COSMO-CLM simulations of the period 1971-2015, at resolutions of 25 km (RCM) and 3 km (CPM) downscaled from ERA-40 and ERA-interim.~~ We validate our simulations against high-resolution observations (EOBS, HYRAS, MSWEP, and UWYO). In the methodology, we present a revisited version of the Precipitation Severity Index (PSI) useful for ~~extremes~~ detection of severe events. Furthermore, we obtain the main modes of precipitation variance and synoptic Weather Types (WTs) associated with ~~extreme~~ heavy precipitation using Principal Component Analysis (PCA). PCA is also used to derive composites of model variables that affect the representation of ~~associated with the thermodynamical processes of~~ heavy precipitation. The results indicate a good ~~detection~~ performance ~~capability~~ of the PSI in the detection of severe events with flexibility to prioritize long lasted events or vents affecting typically drier areas. ~~for precipitation extremes.~~ We identified four WTs as precursors of ~~extreme~~ heavy precipitation in winter, associated with stationary fronts or a zonal flow regimes. In summer, 5 WTs bring heavy precipitation, associated with upper-level elongated troughs over western Europe, sometimes evolving into cut-off lows, or by winter-like situations of strong zonal circulation. The model evaluation showed that CPM (3 km) represents higher precipitation intensities, better rank correlation, better hit rates for extremes detection, and an improved

representation of heavy precipitation amount and structure for selected HPEs compared to RCM (25 km). However, CPM overestimates grid point precipitation rates especially over elevated terrain in agreement with past literature. Composite plots derived from the leading modes of heavy precipitation revealed differences between RCM and CPM in the representation of precipitation amount, that can be as large as 200 mm d^{-1} in either simulation. Nevertheless, RCM simulates systematically more Integrated Water Vapour (IWV) and Equivalent Potential Temperature at 850 hPa than CPM (up to 2 mm and 3 K respectively), due to a wetter mid-level and an intensified emission of latent heat flux over the Sea. At the ground level CPM emits larger latent heat flux than RCM over land, especially in Winter. The consequence is a north to south gradient of surface specific humidity differences. These differences induce an excess of CAPE in CPM over land during Summer compared to RCM. Finally, RCM simulates systematically larger temperature at the surface than CPM, except for some areas of the Po valley and the Italian peninsula during summer. These results show that heavy precipitation is represented very differently in an RCM and CPM set-ups and hence reaching convection resolving resolutions brings added value to study heavy precipitation at decadal time scales.

fostered by the scale dependency of convective dynamic processes such as stronger updrafts and more triggering of convective cells. However, at low altitudes, precipitation differences due to resolution are explained through the scale dependency of thermodynamic variables, where the largest impact is caused by differences in surface moisture up to 1 g kg^{-1}. These differences show a predominant north south gradient where locations north of the Alps show larger (lower) surface moisture and precipitation in CPM (RCM) and locations south of the Alps show larger (lower) humidity and precipitation in RCM (CPM). The humidity differences are caused by an uneven partition of latent and sensible heat fluxes between RCM and CPM. RCM simulates larger emissions of latent heat flux over the Sea (25 W m^{-2} more), and CPM emits larger latent heat over land (15 W m^{-2} more). In turn, RCM emits larger surface sensible heat fluxes over land (30 W m^{-2} more), showing a warmer surface (0.5 to 1°C) than CPM. These results provide evidence that CPM is a powerful tool for obtaining accurate high-resolution climate information also pointing at the different scale dependency of dynamic and thermodynamical precipitation processes at high and low terrain.

1 Introduction

Heavy Precipitation Events (HPEs) cause are one of the main natural hazards affecting Central Europe, often causing tremendous damages and casualties in central Europe (Alfieri et al., 2016; Khodayar et al., 2021; Ranasinghe et al., 2021). The recent event affecting western Germany, Belgium, Netherlands and Luxembourg in July 2021 caused over 170 casualties and losses above 10 bill. Euro (Schäfer et al., 2021). In a warming climate, the occurrence and intensity of such events is projected to increase as assessed in Chapter 8 of the Intergovernmental Panel on Climate Change (IPCC) and previous publications (Douville et al., 2021; Pichelli et al., 2021), due to the intensification of the hydrological cycle (Rajcack and Schär, 2013; Ban et al., 2018). Such events may occur both during winter and summer fostered by Deep Moist Convection (DMC), a large

65 vertical transport of precipitating air masses (Emanuel; 1994). In Winter, ~~extreme~~ heavy precipitation typically occurs under strong synoptic forcing (Keil et al., 2020), caused by the large-scale advection of positive vorticity in cold upper-level layers (Holton, 2013). The associated synoptic patterns have been studied in past literature (e.g. Knippertz et al., 2003; Werner and Gerstengarbe, 2010; Stucki et al., 2012) referring a strong influence of northerly cut-off geopotential lows and elongated troughs as well as of the Atlantic zonal flow. In summer, DMC is often triggered by favourable local and mesoscale conditions

70 close to the surface, including an ~~energetic~~ warm and moist low-level and a triggering mechanism (Doswell, 1996). When these conditions coincide with the arrival of a mesoscale low-pressure system, highly damaging precipitation is likely to occur~~. Summer HPEs are hence characterized by strong, localized, and short convective showers that have a high risk of causing flash flooding (Doswell et al., 1996; Khodayar et al., 2021).~~

Understanding heavy precipitation processes, their variability and trends at the ~~climate scale~~ decadal time scales is ~~thus~~ needed

75 to provide better prevention and adaptation strategies. Considering modelling approaches, dynamical downscaling with regional climate models (RCM) has proven to be an important tool towards this end ~~, even though convection is parameterised~~ (e.g. Jacob et al.,2013). Recently, the development of Convection-Permitting Models (CPMs) led to a ~~further~~ step forward (Coppola et al., 2018; Prein et al., 2020; Lucas-Picher et al., 2021). ~~. The added value of CPM lies~~ since a parametrized description of deep convection is no longer needed. ~~primarily due to in the~~ An explicit representation of convection is often

80 applied for horizontal grid spacings ~~. This occurs when~~, provided a horizontal resolution ~~higher~~ lower than ca. 5~~3~~ km. ~~is attained.~~ Also improved is the representation of the model's land type, use and elevation (Prein et al., 2015; Heim et al., 2020). These advancements led to improvements in representing the daily precipitation's diurnal cycle (Kendon et al., 2012; Berthou et al., 2018; Ban et al., 2021); its structure, intensity, frequency, and duration (Berthou et al., 2019; Berg et al., 2019); its sub-hourly rates (Meredith et al., 2020); and orographic triggering (Ban et al., 2018). These improvements are consistent over the

85 main modelling regions worldwide. However, not all problems are solved, since CPMs have also shown relevant wet biases, inducing an overestimation of extreme intensities (Kendon et al., 2012). CPM uncertainties arise from shortcomings in the physical parameterizations, the coupling of the numerics and the physics-dynamics, deficiencies in the representation of the initial conditions and the lack of sufficient high-resolution observations for validation (Lucas-Picher et al., 2021).

90 Particularly relevant for the improvement of heavy precipitation in CPM is the better representation of DMC processes, ~~the dynamical processes of DMC,~~ especially when convection is triggered close to the surface (Bui et al., 2018). In fact, several studies have shown that CPMs induce stronger updraughts that leads to stronger convection ~~and thus larger precipitation than coarse resolution models~~ (Meredith et al., 2015a; Meredith et al., 2015b). This is also observed in Numerical Weather Prediction (NWP) simulations (Barthlott and Hoose, 2015; Panosetti et al., 2018). When convection occurs over an area of

95 complex orography, the finer representation of the mountains in CPM increases the triggering of convection (Langhans et al., 2012; Vanden Broucke et al., 2018; Heim et al., 2018; Vergara-Temprado et al., 2020), leading to a better agreement with radar observations (Purr et al., 2019).

Regarding ~~other model variables, the scale-dependency of thermodynamical precipitation processes,~~ previous papers argued that CPM~~s~~ improve the simulation of surface temperature (Ban et al., 2014; Prein et al., 2015; Hackenbruch et al., 2016), due to a better representation of the orography, as well as ~~the precipitation's location and~~ the cloud coverage (Lucas-Picher et al., 2021). Hohenegger et al., (2009) showed that using CPM favours a negative soil-precipitation feedback (more rain under dry soil conditions), as opposite to convection-parameterized RCM (25 km), which show a positive feedback (more rain under wet soil conditions). The negative bias in CPM is due to stronger thermals in CPMs given dry soil conditions, thus initiating convection (Hohenegger et al., 2009). Moisture biases also affect the development of ~~extreme~~ heavy precipitation where a wet bias was found for established RCM models (Lin et al., 2018; Li et al., 2020), as well as in CPM simulations (Risanto et al., 2019; Bastin et al., 2019; Caldas-Alvarez and Khodayar, 2020; Li et al., 2020). However, how both RCM and CPM deal with the moisture ~~excess~~ wet bias still is an open question. Regarding atmospheric instability Li et al., (2020), found larger Convective Available Potential Energy (CAPE) during the afternoon in CPM, which was correctly converted to larger precipitation at the Tibetan Plateau. ~~However, more knowledge on the interplay of moisture and instability in CPM at the European continent is needed.~~ Finally, the scale dependency of other variables of interest for convective development such as Equivalent Potential Temperature at 850 hPa (θ_e^{850}), has been seldom investigated.

The model ~~assessed~~evaluated in this paper is the COnsortium for Small scale Modelling in Climate Mode (COSMO-CLM; Schättler et al., 2016, Rockel et al. 2008) which is especially suitable for studying differences between RCM and CPM due its flexibility for configuration in convection parametrized and convection permitting resolutions. ~~COSMO-CLM is a non-hydrostatic model using the fully compressible atmospheric equations (Schättler et al., 2016), incorpooratinbg sub-grid turbulence, convection and grid scale clouds and precipitation parameterizations.~~ ~~It also uses a soil model called TERRA-ML (Doms et al., 2011) to parametrize the mass and heat exchanges between the surface and the atmosphere (Rockel et al., 2008).~~ COSMO-CLM is a well-established regional climate model used by several research and applied-science institutions in Europe (Sørland et al., 2021) and hence there is interest in knowing ~~what the implications of reaching CPM resolutions are for the different model variables.~~how it simulates heavy precipitation and associated processes in a CPM set-up.

One established technique to work with large data sets, such as decadal climate simulations is Principal Component Analysis (PCA). PCA ~~Provided the large amount of data involved in climate studies as the one presented here, Principal Component Analysis (PCA)~~ is a powerful method to reduce the dimensionality of a set (Joliffe, 2022) and ~~be able~~ to extract~~work with~~ the principal underlying features. One of its applications is the derivation of the leading spatial patterns of atmospheric fields during specific situations, e.g., heavy precipitation (Knippertz 2003, Sergina et al., 2020). Provided PCA, also calculates the correlation between the days of the set and the derived spatial pattens, it can be used to construct ~~categorized the days of the set and obtain~~composite maps of relevant model variables associated with the respective spatial patterns of a specific model variable, e.g., ~~precipittion~~precipitation. Although PCA has been used for these applications in the past, to our ~~knowledge, no studies exist using composite maps obtained from PCA to~~knowledge it has not been applied to study model differences between RCM and CPM.

Comentado [FH(1):] Moved to 2.2

Con formato: Fuente de párrafo predeter., Fuente: (Predeterminada) Times New Roman, 10 pto, Color de fuente Automático, Diseño: Claro

Con formato: Fuente: (Predeterminada) Times New Roma Color de fuente: Automático

Con formato: Fuente: (Predeterminada) Times New Roma Color de fuente: Automático

Con formato: Fuente: (Predeterminada) Times New Roma Color de fuente: Automático

Con formato: Fuente: (Predeterminada) Times New Roma Color de fuente: Automático

Con formato: Fuente: (Predeterminada) Times New Roma Color de fuente: Automático

Con formato: Fuente: (Predeterminada) Times New Roma Color de fuente: Automático

Con formato: Fuente: (Predeterminada) Times New Roma Color de fuente: Automático

The aim of this work is to evaluate reanalysis-driven RCM (25 km) and CPM (3 km) decadal long simulations of the greater Alpine area in the period 2000-2015 and assess the~~ir~~ differences in representing heavy precipitation ~~situations~~and associated environments. ~~scale-dependency of thermodynamical processes influencing extreme precipitation, focusing on the period 1971 to 2015. Particular research questions that we would like to answer are, how~~ whether we ~~can we better detect precipitation extremes? And what can we assess the~~ large-scale variability and main synoptic patterns ~~are~~ associated with ~~the detected extremes.~~ events? ~~Finally we would like to assess the model differences between RCM and CPM in representing variables such as atmospheric and soil moisture, surface heat fluxes , CAPE and surface wind convergence.highlight the differences Such varibalbes influence the occurrence of heavy precipitation, especially for events with a weak synoptic forcing. How is heavy precipitation representation affected by the use of CPM? How much are processes such as energy and moisture fluxes, instability or surface fluxes affected by CPM?~~

This paper is organized as follows: i~~i~~n Sect. 2 we introduce the dataset and methods employed; in Sect. 3 we present the main

synoptic weather types bringing ~~extreme~~ heavy precipitation; in Sect. 4 we evaluate ~~extreme~~ heavy precipitation intensity and occurrence in the climate simulations; in Sect. 5 we validate precipitation, humidity, and temperature fields of selected ~~extreme~~ heavy precipitation events; in Sect. 6 we introduce the spatial patterns of precipitation derived from PCA, In Sect. 7 we present the differences of precipitation composites and in Sect. 8 we do the same for other model variables relevant for precipitation representation. ~~we assess the scale dependency of moisture and energy fluxes, instability, and soil-atmosphere fluxes. Finally in Sect. 7 we present our conclusions.~~

2 Data and methods

2.1 Observational datasets

We use observations from different sources for validation and comparison of the climate simulations (Tab. 1). We employ ~~T~~the Ensembles OBSservations (EOBS) gridded precipitation and relative humidity at the surface (*hurs*) products at 25 km resolution (EOBS-25km) which are provided by the European Climate Assessment & Dataset (ECAD) centre at ~~0.1° (ca. 11 km) and~~ 0.25° (ca. 25 km) of spatial resolution~~s~~ for the period 1950-2020. We use v.22.0e (Dec 2020)~~,~~ employing ~~where EOBS-25km employs~~ a 100-member ensemble created through stochastic simulations based on interpolated station data from national institutions including 9000 rain gauges (Cornes et al., 2018). ~~The 25 km resolution and daily aggregations are used for validation of precipitation simulations for 1971-2015 to match the resolution of the evaluated RCM simulation (Fig.1).~~ EOBS-25km has been widely used in previous literature for validation purposes (e.g., Tramblay et al., 2019; Bandhauer et al., 2021) and has been shown to have low median absolute biases with respect to other regional European precipitation products such as CARPATCLIM or Spain02 (Cornes et al., 2018).

The HYdrologische RASterdatensaetze (HYRAS) gridded precipitation dataset, provided by the German Weather Service (DWD) is available at 1 km (ca. 0.01°), 5 km (ca. 0.05°) and daily resolution. HYRAS covers Germany and neighbouring catchments in parts of Switzerland, Austria, the Netherlands, France, Belgium, and Poland (Fig.1). The version v2 covers the

period 1951-2015 and was derived using multiple linear regression and inverse distance weighting interpolation of 6200 rain gauges considering the orography (Rauthe et al., 2013, Razafimaharo et al., 2020). HYRAS has a very high quality and its ~~in extreme precipitation observations compared to the European Centre for Medium-Range Weather Forecasts REanalyes, 5th generation (ERA-5) and EOBS-25km (Hu et al., 2020).~~ ~~Its~~ high-resolution enables a good representation of local scale features, outperforming the coarse resolution of EOBS-25km (Hu et al., 2020).~~.~~ However~~.,~~, it is only available over Germany and nearby catchments.

The Multi-Source Weighted-Ensemble Precipitation (MSWEP) is a gridded precipitation product provided by GloH2O (http://www.gloh2o.org/) at 0.1° (ca. 11 km) spatial resolution and 3-hourly temporal resolution for the period 1979-2020 with global coverage. We use version v.2.2.0. ~~MSWEP~~ which was obtained through weighted interpolation of different observations to a common grid. It merges data from rain Gauge observations from Climate Prediction Center (CPC) unified and Global Precipitation Climatology Centre (GPCC), satellite observations from the CPC MORPHing product (CMORPH), Global Satellite Mapping Precipitation Moving Vector with Kalman (GSMaP-MVK) and Tropical Rainfall Measuring Mission Multi-Satellite Precipitation Analysis (TMPA) 3B42, as well as two reanalyses datasets ERA-interim and Japanese Reanalyses JRA-55 (Beck et a., 2019). MSWEP has a high~~er~~ median correlation (up to 0.67) against stations, compared to CMORPH (0.44) and TMPA-3B42 (0.59) (Beck et al., 2017). We use the MSWEP product to profit from its high accuracy, shown in previous studies, globally (Beck et al., 2017, 2019; Xiang et al., 2021) as well as in specific geographies (Du et al., 2022; Peña-Guerrero et al., 2022). MSWEP has the advantage of covering sea surfaces and is adequate for precipitation event evaluation because it includes ~~station~~gauge data from CPC and GPCC. ~~and to overcome the limitations of HYRAS-5km (limited spatial coverage) and EOBS-25km (land-only).~~

The radiosonde data archived by the University of Wyoming (UWYO) are used to validate the RCM and CPM humidity and temperature profiles. The stations are located close to large European cities, with an average distance of 250 km between stations. The temporal resolution ranges between 6 h, 12 h and 24 h and~~,~~ ~~T~~the provided information includes height, atmospheric pressure, temperature, and dew point temperature on ca. 30 levels. ~~between 1000 and 300 hPa, as well as integrated convective indices. The~~ The UWYO soundings have~~are~~ often been used as reference for validation studies (e.g., Ciesileski et al., 2014; Yang et al., 2020).

2.2 ~~Methodology: Performance Comparison performance~~Setup of the COSMO-CLM RCM and~~vs~~ CPM simulations

In this work we use simulation with COSMO-CLM is a non-hydrostatic model using the fully compressible atmospheric equations (Schättler et al., 2016), incorporating sub-grid turbulence, convection and grid scale clouds and precipitation parameterizations. It also uses a soil model called TERRA-ML (Doms et al., 2011) to parametrize the mass and heat exchanges between the surface and the atmosphere (Rockel et al., 2008).

Here, we systematically compare reanalysis driven regional climate simulations with COSMO-CLM how they represent heavy precipitation events at typical RCM resolution (e.g. 10 km – 50 km; hereafter named RCM) and at convection permitting resolution (~ 3 km, named CPM).

All simulations were performed with the version COSMO-CLM5 and use a setup optimized for the specific resolution.

~~It also uses a soil model called TERRA-ML (Doms et al., 2011) to parametrize the mass and heat exchanges between the surface and the atmosphere (Rockel et al., 2008).~~

The RCM simulation (Tab.2) has a grid spacing of 0.22° (ca. 25 km), a 3-hourly output, and was performed within the scope of the MiKliP project (Feldmann et al., 2019) over the period 1961 - 2018. This simulation was performed for the Euro-CORDEX domain (Jacob et al., 2014) and thus covers the European continent and vast areas of the North Atlantic and the Mediterranean (Fig.1). The RCM simulation is forced by ERA-interim (Dee et al., 2011) for the main period of interest. The setup equals the recommend setup for COSMO-CLM5 for typical RCM resolutions. The most relevant model settings are summarized in Tab. 2 and in Sørland et al., 2021.

The CPM simulation uses a higher COSMO-CLM5 subversion with a few bug-fixes and additional output variables. The setup has been optimized for convection permitting scales and is used in the CORDEX Flagship Pilot Study on Convection (Coppola et al., 2018) and the simulation has been evaluated in Ban et al. (2021). There are to some differences in resolution specific tuning parameters, but the main difference is the switching of the deep-convection parametrization (Tiedtke; 1989; Baldauf et al.; 2011; cf. Tab. 2). The simulation is performed by downscaling the RCM simulation described above over the grater Alpine area (ALP-3 domain, with a 3km (0.0275°) resolution for the period 2000 – 2015.

Another CPM simulation – here called KLIWA-2.8km (cf. Tab. 2) – is used auxiliary just in chapter 4 and Figure 5 to extend period for the comparison of the historical events. The grid spacing of this simulation is 2.8km (0.025°) and a smaller modelling domain covering southern Germany and the Alps (cf. Fig. 1) for the period 1971-2000. It is forced by ERA40 re-analysis (Uppala et al., 2005) in a three-step nesting approach (Hundhausen et al., 2022). This simulation uses a slightly older subversion missing a few bug fixes. The main differences to CPM can be found in Tab. 2.

Con formato: Normal

~~We systematically compare regional climate simulations with the Consortium for Small-scale MOdeling (COSMO) model in CLimate Mode (CCLM).COSMO-CLM between 2000 and 2015of the recent climate at two model resolutions; 25 km, hereafter named RCM and 3 km, named CPM. In the latter, deep convection is explicitly resolved. Besides precipitation, we asses the differences in other model variables, proxies of processes relevant for the initiation and development of heavy precipitation, such as surface heat fluxes humidity and temperature, Convective Available Potential Energy (CAPE), or outgoing longwave radiation. surface heat fluxes, or low-level wind convergence.~~

~~The RCM simulation (Tab.2) covers the period 1961-2018, has a nominal grid spacing resolution of 0.22° (ca. 25 km), a 6-hourly output, and was performed within the scope of the finalized project MiKlip phase II (Feldmann et al., 2019). This simulation was performed for the Euro-CORDEX domain (Jacob et al., 2014) and thus covers the European continent and vast~~

areas of the North Atlantic and the Mediterranean (Fig.1). The RCM simulation is forced by ERA-40 Reanalysis (Uppala et al., 2005) until 1979 and by ERA interim (Dee et al., 2011) for the period of interesterest. vailability these data sets. The physical packages and model settings are consistent throughout the whole period 1961-2018. The most relevant model settings are summarized in Tab. 2 and in Feldmann et al., (2019), these include [**add info on the RCM simulations**].

The CPM simulation (Tab. 2) is built up from two separate simulations (Tab. 2). The first one is the KLIWA 2.8km simulation, which spans the period 1971 to 1999, is forced by ERA-40, has a 0.025° resolution (ca. 2.8 km), a 6-hourly output, covers the region of southern Germany and Switzerland (Fig.1b) and was performed for the "Klimaveränderung und Wasserwirtschaft" (KLIWA) project (Hackenbruch et al., 2016). The is obtained from the Flagship Pilot Study (FPS) Convection program (Coppola et al., 2018) funded by the World Climate Research Programme (WCRP). It is second simulation ALP 3 simulation spans from 2000 to 2016, is forced by ERA-interim, has a resolution of 0.0267° (ca. 3km), a 6 hourly output and , covers the greater Alpine area (Fig.1b).), is part of the Flagship Pilot Study (FPS) Convection program (Coppola et al., 2018) funded by the World Climate Research Programme (WCRP). A detailed description of CPM can found in . Table 2 sumarizes the most relevant physical parameterizations used, the [**add info for the CPM simulation, Highlight the inactive deep conv. Param.**]

Both CPM simulations have the same model dynamics, the same integration time step (20 seconds), the same grid type (Arkawa-C), the same output frequency (6 hourly) and the same active parameterizations. The physical parametrizations are the same as in RCM, except for the convection parametrization which is restricted to shallow convection (Schättler et al., 2016). However, KLIWA 2.8km and ALP-3 differ in the number of vertical levels (30 vs 40), the spatial resolution (2.8 km vs 3 km), the forcing data (ERA-40 vs ERA interim), and the simulation domains (Fig. 1). In spite of these small inconsistencies, we combine both CPM simulations to attain a sufficiently large investigation period for comparison with the RCM simulation and observational datasets.

Additionally, we use the KLIWA 2.8km simulation (Tab. 2 and Fig. 1) to complement CPM in the study of COSMO-CLM's detection capabilities (Sect. 4, Fig. 6). KLIWA 2.8 is used auxiliary to extend the analysed period to the year 1971. KLIWA 2.8km is forced by ERA 40, has a 0.025° resolution (ca. 2.8 km), a 6 hourly output and covers the region of southern Germany and Switzerland (Fig.1b). This siumulation was obtained in the "Klimaveränderung und Wasserwirtschaft" (KLIWA) projeet (Hackenbruch et al., 2016) and used three nests at 0.44 °,0.0625 °, and 0.025°. [**add info for the CPMLIWA-2.8 simulation**].

Although CPM and KLIWA 2.8km are not identical, they have a similar horizontal resolution (0.0267° and 0.025° respectively), they use the same model, the same integration time step (20 seconds), the same grid type (Arkawa-C), the same output frequency (6 hourly) and the same active parameterizations, e.g., [add actie shared parameteriyations]. Conversely, KLIWA 2.8km and CPM differ in the number of vertical levels (30 vs 40), the forcing data (ERA-40 vs ERA interim), and the simulation domains (Fig. 1). These is tolerated in the analysis of the model's detection capbpability in Fig. 6 to profit from

260 ~~a larger investigation period of 45 years.~~ ~~We concede these inconsitensies to extend the investigation period to 45 years, exclusively for the study of the historical heavy precipitation events (Fig. 6).~~

Two areas are investigated in our study. The first, denominated southern Germany (SGer, Fig.1) encompasses the northern Alps, and southern Germany up to North-Rhein-Westphalia and Saxony. ~~, is used to provide a validation of precipitation for the complete period 1971-2015 (Sect. 4)~~. This area is ~~and period were~~ selected to~~as it~~ fulfil the requirements of ~~all~~ the modelling and observational data sets (availability, coverage, time span). The second area, ~~ALP-3~~CPM (Fig. 1), covers the greater Alpine domain including the northern Mediterranean basin and is used for comparison of the model performance RCM vs. CPM. ~~validation of HPEs and the in-depth analysis of the scale-dependency of precipitation-related variables for the period 2000-2015 (Section 6).~~

2.3 Analytical methods

2.3.1 The Precipitation Severity Index (PSI)

We ~~employ~~ re-adapted the PSI, an index previously used to detect ~~the extreme~~ heavy precipitation events (Piper et al., 2016) and severe wind storms (Leckebusch et al., 2008; Pinto et al., 2012) to include precipitation persistence. By doing so we can consider ~~including~~ three different, but intertwined aspects of ~~extreme~~ heavy precipitation: grid-point intensity, spatial extent of affected area and ~~time~~ temporal persistence. ~~The PSI is adapted from the Storm Severity Index (SSI; Leckebusch et al., 2008; Pinto et al., 2012) and further developments by Piper et al., (2016).~~ It is re-defined as follows:

$$PSI_T = \frac{1}{(1+d)\cdot A} \sum_{i=1}^{N} \sum_{j=1}^{M} \sum_{t=T-d}^{T} \frac{RR_{ijt}}{RR_{perc_{ij}}} \cdot (\Delta x)^2 \cdot \prod_{\tau=t}^{T} I\left(RR_{ij\tau}, RR_{perc_{ij}}\right) \quad \text{[1]}$$

$$I\left(RR_{ij\tau}, RR_{perc_{ij}}\right) = \begin{cases} 0 \ if \ RR_{ij\tau} \leq RR_{80_{ij}} \\ \\ 1 \ if \ RR_{ij\tau} > RR_{80_{ij}} \end{cases}$$

280

The PSI values at a certain time step T (PSI_T) are obtained from~~depends on~~ the ratio between grid point daily precipitation (RR_{ijt}) and a user-defined threshold. ~~percentile of the climatology ($RR_{perc_{ij}}$). In this paper w~~We set this threshold to be the 80-percentile ($RR_{perc_{ij}}$) to ~~ensure that only precipitation events with high grid-point intensity are considered. We thus~~ neglect grid points whose precipitation is lower than the set threshold one for day T ($RR_{ij\tau} \leq RR_{perc_{ij}}$). This is done~~,~~ by means of the function $I\left(RR_{ij\tau}, RR_{perc_{ij}}\right)$. We consider the spatial extent by summing the ratios over the spatial extent ($N x M$) of the study region along the directions i and j. The ratios are multiplied by the area of one grid cell $(\Delta x)^2$. The precipitation persistence is considered in the calculation through the sum over time (t). The ratios at each grid point for day T and the previous d days ($d = 2$ in our case) are added for the PSI calculation, provided precipitation was continuous and larger than $RR_{perc_{ij}}$ at that same grid point i, j. ~~To consider the size of each grid cell we multiply by the area of one grid cell $(\Delta x)^2$. Finally, the ratios are~~

290 ~~summed over the spatial extent (*NxM*) along directions *i* and *j*.~~ The daily PSI value is normalized to the area of the simulation domain $A = N \cdot M \cdot (\Delta x)^2$ multiplied by $(1 + d)$ to consider the addition of grid points with persistent precipitation. Prior to the PSI calculation, we include a correction for latitude stretching of the grid as $sqrt(cos(lat))$ following (North et al., 1982).

To assess the performance of the PSI, we calculate Spearman's rank correlations between the PSI and a simpler field sum index ($fldsum$). We use daily precipitation data from HYRAS-5km between 01-Jan-1971 and 31-Dec-2015 over the

295 investigation area SGer (Fig. 1). We test different combinations of the PSI parameters $RR_{perc_{ij}}$ and d (Eq. 1). Fig. 2 shows the rank correlations against $fldsum$ and the three top-ranked events of each implementation and the daily precipitation of the 22-Oct-1986 event.

We find a high rank correlation between the PSI and $fldsum$ for low values of $RR_{perc_{ij}}$ and d. For instance, when we set $RR_{perc_{ij}}$ as the percentile-80 of the 1971-2015 period and $d = 0$ (equivalent to considering no persistent precipitation) the

300 rank correlation is 0.97, indicative of a very similar functionality between the PSI and $fldsum$ (Fig. 2a). For instance, in this configuration the third event in the ranking differs between the PSI (20-Dec-1993) and $fldsum$ (20-Nov-2015). The reason behind is that the 20-Dec-1993 (supplementary material) event occurred over a flat area, unfrequently affected by heavy precipitation. The PSI prefers this event to 20-Nov-2015 (affecting mainly complex terrain) because the threshold set to the 80-percentile is easier to surpass over flat terrain.

305 . As we increase $RR_{perc_{ij}}$ and d, the rank correlation decreases, implying a different ranking of the events (Fig. 2a). For example, a percentile-95 for $RR_{perc_{ij}}$ and $d = 2$ brings a rank correlation of 0.86 which favours the detection of events with larger grid-point intensity and temporal persistence. For illustration, the 22-Oct-1986 event (Fig. 2b, c, d) is ranked as the most severe event in the period in this configuration due to precipitation totals between 50 mm d^{-1} and 150 mm d^{-1} impacting for three consecutive days the same areas, e.g., the Colmar region or the Marburg-Siegen area (see Fig.2, b, c, and d). The

310 remainder events can be seen in the supplementary material.

To conclude, the advantage of the PSI with respect to a simpler field sum index is its capability to detect rarer and more persistent events. Rarer events can be found because the threshold $RR_{perc_{ij}}$ guarantees the selection of events where either heavy precipitation falls over climatologically drier areas or where extreme intensities take place over typically wet areas (e.g., complex terrain). For its part $d = 2$ favours the detection of events where heavy precipitation occurred continuously on the

315 same grid point up to a maximum of wo days. That said, a low percentile threshold ($RR_{perc_{ij}}$) or $d = 0$ will bring a functionality no different to $fldsum$. This makes the PSI a flexible solution that can be tailored to the user´s needs. Finally, the PSI is also flexible to set the threshold $RR_{perc_{ij}}$ to a fixed amount, e.g., 120 mm d^{-1}, to ensure that only grid points above that threshold will be included in the calculation. This is a possible configuration that could be used in future studies.

To assess the performance of the PSI in detecting HPEs, we calculate Spearman's rank correlations between PSI values and a simpler field sum index ($fldsum$). We use daily precipitation data from HYRAS between 01 Jan 1971 and 31 Dec 2015 over the investigation area SGer in southern Germany and the Alps (Fig. 1). We test different settings of the PSI, namely analyse in detail the exceptional heavy precipitation season of spring 2007 in southern Germany and the Alps (Schacher et al., 2007). Figure 2 shows the temporal evolution of daily PSI values at SGer for different settings of the percentile in $RR_{perc_{tj}}$ and of the persistence parameter (d) parameters in Eq. 1.

We found a variable rank correlation between the PSI and fldsum as we modify the values of $RR_{perc_{tj}}$ and d. The lower $RR_{perc_{tj}}$ and d, the larger the rank correlation between the PSI and fldsum. For instance when we choose $RR_{perc_{tj}}$ as the percentile 80 and $d = 0$ (equivalent to considering no persistent precipitation) the rank correlation is 0.97, indicative of a similar functionality between the PSI and $fldsum$. As we increase $RR_{perc_{tj}}$ and d, the rank correlation decreases implying a different ranking of the events. For $RR_{perc_{tj}} = 90$ and $d = 2$ the rank correlation is 0.96 and for $RR_{perc_{tj}} = 95$ and $d = 2$ the correlation is 0.86. Using the PSI in the latter configuration instead of a simpler sum field index favours the detection of events with larger grid-point intensity and temporal persistence.

For illustration we show in Fig.?? the top 5 precipitation events detected with the fldsum index and the previously mentioned configurations of the PSI. We see that ranks as top event and that events such as, Additionally, the temporal evolution of the field sum ($fldsum$) is shown. The PSI detects the six HPEs affecting SGer during the season, namely, on the 08 May, 14 May, 28 May, 14 Jun, 22 Jun, and 25 Jun (Fig. 2). For a fixed value of the percentile ($perc = 80$), the impact of considering persistent precipitation during the two days prior to the analysed date (perc 80 days 2; black) is to reduce the PSI values and to shift the peaks to the last day of the event (see events 1, 3, and 5), compared to considering no days of persistent precipitation (perc 80 days 0; dark grey). On the other hand, for a fixed value of the persistence parameter ($d = 2$), increasing the percentile (perc 95 days 2; light grey) does not affect the timing of the temporal evolution, but reduces the PSI values and neglects episodes of stratiform rain (11 Jun). This analysis provides confidences that the selected parameters $perc = 80$, and $d = 2$, are suitable for summer and winter extremes detection, not to neglect all stratiform precipitation events and to identify cases where precipitation occurs over already very wet areas.

The comparison against $fldsum$ (dashed line), shows high spearman's rank correlations of the PSI, between 0.97 and 0.86, depending on the $perc$ and d parameters. This implies that the PSI detects events ranked by highest maximum areal precipitation covering the functionality of $fldsum$. However, the PSI (perc 80 days 2; black) can help neglect weaker episodes such as the 11 Jun precipitation. Fig. 2 shows the 90-percentile of the 1971-2015 climatology over SGer for the PSI (black horizontal line), and the $fldsum$ (dashed horizontal line) as a plausible threshold to detect extremes. Whereas the stratiform event of 11 Jun belongs to the 90-percentile of $fldsum$, it is neglected by the PSI, that only identifies events of very high grid-point intensity.

350 ~~Two remarks,~~

~~- PSI with d=2 favours persistent perciptiation over a lot of grid points.~~

~~- Persistenvce adds severity, notion of persisnte precipitation much more leading to flooding~~

~~- Luego PSI te ofrece flexibilidad si uno quiere eventos de mas de x mm/d lo puedes elegir tú, en mi ejemplo un 95 es~~
355 ~~equivalente a qué? Hay que verlo, También es un percentil sobre el punto, lo que puede ser extremo o raro en un sitio no tiene~~
~~por que serlo eeverywhere.~~

~~También tener en cuenta que es un índice estadísitico… lo que es raro para un punto puede no serlo para otro…~~

~~We conclude that the PSI is more useful than $fldsum$ for detection of events with high grid-point intensity and persistent~~
360 ~~precipitation if high precipitation thresholds ($RR_{perc_{ij}}$) and $d \neq 0$ are set. However, for low thresholds and $d = 0$ its~~
~~functionality resembles that of the simpler $fldsum$ index which is less complex to implement.~~ ~~is a suitable index for extreme's~~
~~detection that adds value with respect to a simpler field sum by favouring the detection of events with large grid point intensities~~
~~and persistent heavy precipitation.~~

2.3.2 Principal Component Analysis

365 Principal Component Analysis (PCA) is a method to reduce the dimensionality of a data set, by transforming it to a new coordinate system of variables called Principal Components (PCs; Joliffe, 2002). The functions that allow the transformation from the original set to the PCs space are called Empirical Orthogonal Functions (EOFs). The transformation is performed in such a way that the explained variance is concentrated in a small number of the new variables. By construction, the leading EOF1 has the largest explained variance, followed by EOF2, ~~-~~and so on. In this paper, we investigate the PCs and EOFs of
370 500 hPa geopotential height fields (Sect. 3.1) and daily precipitation (Sect. 6~~5~~). Similarly to Ulbrich et al., (1999), we obtain EOFs representing the spatial patterns of the target variable, that account for the main modes of variance. On the other hand, the PCs are time series which provide the information of the ~~loading~~ correlation of each EOF ~~at~~ to a specific ~~time~~ day in the ~~series~~step.

Given that the explained variance is now concentrated in a small number of variables, it is important to discern how many
375 EOFs should be retained. With this aim, we use a method of parallel analysis based on the randomization of eigenvalues named the random-λ rule (Peres-Neto, 2005). The procedure is as follows, 1) a random data array is created with the same dimensions as the data array under study, 2) PCA is applied on the random array, 3) steps 1 and 2 are repeated up to 1000 times, retaining ~~at~~ the eigenvalues showing a significance over 95 % (alpha= 0.05). 4). If the original eigenvalues exceed the critical values from the random data, then we reject the null-hypothesis (Peres-Neto, 2005). The random-λ rule is more suitable than other

380 methods of parallel analysis such as the N-rule (Preisendorfer and Mobley, 1988) since it does not assume a normal distribution for the array of random values and thus works better for variables such as precipitation.

2.3.3 Validation metric Fractions Skill Score

The Fractions Skill Score (FSS) provides an estimation of the model's skill in representing the fraction of surface affected (or not) by heavy precipitation (Skok and Roberts, 2016). A perfect forecast has thus an FSS of 1. A simulation with no skill has

385 an FSS of 0. In this work, we set a threshold of 40 mm d^{-1} to define structures affected by heavy precipitation. The threshold is in the range of values implemented by Roberts and Lean (2008) for simulations of spring convective rain over southern England. We select this threshold to be able to identify clear precipitation structures otherwise masked by the choice of a too large or too low threshold analogously to Caldas-Alvarez et al., (2021). Equation 2 defines the FSS following Roberts and Lean (2008).

390 $$FSS = 1 - \frac{\frac{1}{M}\sum_{i=1}^{M}(f_{mod}-f_{obs})^2}{\frac{1}{M}(\sum_{i=1}^{M}f_{mod}^2+\sum_{i=1}^{M}f_{obs}^2)} \qquad [2]$$

The fractions of surface affected by heavy precipitation are represented by f_{obs} and f_{mod}, for the observations and the model, respectively. Both are calculated as the number of grid points affected by precipitation over the defined threshold (40 mm d^{-1}) divided by the total number of grid points of a domain. FSS is computed as the ratio of the sums of fraction differences for M sub-boxes within the investigation domain. These M sub boxes are defined as sub-domains around M grid points with N near

395 neighbours. N in our case is 12 since most of the events we validate have shown a skill larger than the target skill defined as $FSS_{target} = 0.5 + f_{obs}/2$ for $N = 12$. For detailed explanation, refer to Roberts and Lean (2008), Skok et al., (2016), and Caldas-Alvarez et al., (2021).

3 Synoptic weather types

We obtain the predominant large-scale situations associated with heavy precipitation applying PCA. We analyse the EOFs of

400 geopotential height at 500 hPa, based on the RCM simulation, for the period 1971-2015. We select dates of heavy precipitation in the 98-percentile of severity (PSI) in the HYRAS-5km data set over the investigation region SGer (Fig. 1). Figures 3 and 4 provide, respectively, the dominating weather types of ~~extreme~~ heavy precipitation for summer (MAMJJA) and winter (SONDJF). The comparison against the CPM is not shown here since only negligible differences exist with respect to RCM. This is because the boundary conditions from the forcing reanalyses (ERA) strongly determine the large-scale features under

405 play (Prein et al., 2015).

In winter, four synoptic patterns of 500 hPa geopotential height suffice to explain the natural variability, following the random-λ rule with a 95% significance in the t-test (Peres-Neto et al., 2005). They account for 74% of the heavy precipitation episodes. The first mode, representing 29 % of the events, is characterized by wave trains of low pressure associated with northerly

incursions of polar air (Fig. 3). The synoptical situation is analogue to the Stationary Fronts (STF) category proposed by Stucki et al., (2012). In this situation, heavy precipitation over the Alps is associated with strong upper-level lifting over northern Italy and large southwesterly advection of moisture from the Mediterranean. Historical cases belonging to this category, as identified by the PCA, are the second phase of the 23-31 October storms in 1998 (Fuchs et al., 1998) or the late November events in 2015 (Tab. 3, https://www.wetter.de/cms/so-war-das-wetter-im-november-2015-2566771.html), for instance. The second mode, accounting for 22 % of the events, shows strong north-south gradients of the 500 hPa height and fast zonal circulations (Fig. 3). This synoptic pattern has been identified as a Zonal Flow (ZOW; Stucki et al., 2012) or as a narrow and elongated streamer (Massacand et al., 1998). The zonal circulation favours moisture advection from the Atlantic and can produce large precipitation in non-convective environments (Stucki et al., 2012). The 29 December 2001 event belongs to this precipitation mode, for instance. The third and four modes account for 12 % and 11 % of precipitation episodes, respectively and show similarities with the 500 hPa geopotential heights of the second mode (Fig. 3). However, the third synoptic pattern shows a weaker Azores high, favouring the advection of Atlantic moisture with a southwesterly component. The fourth mode, for its part, shows a weaker polar low, which favours the development of anti-cyclonic circulation (Fig. 3).

In summer, five synoptic patterns of 500 hPa geopotential height are discernible from random noise (Peres-Neto et al., 2005), accounting for 77 % of the events. The first mode, corresponding to 27% of the considered dates, shows an extended upper-level trough from the British Isles down to southern France (Fig. 4). This configuration shows elements of an Elongated Cut-Off (ECO) and of CAnarian Troughs (CAT; Stucki et al., (2012). In such situations upper-level lifting occurs east of the trough together with southerly moisture advection either from the southwest or the southeast, respectively. Such situation occurred for instance during the first stages of the large central European flooding of early June 2013 (Klemen et al., 2016). If a blocking situation occurs, for instance Omega blocking, the persistence of precipitation is enhanced and can lead to recurrent events (Kautz et al., 2021) at the eastern flank of the ECO or CAT . The second summer precipitation mode (Fig. 4), accounting for 19% of the events, presents a similar pattern to the third and four modes of winter precipitation (Fig. 3) with the characteristic strong zonal flow from the Atlantic. Examples of this synoptic configuration are the March 1988 events flooding the Rhein river (southern western Germany; Prellberg and Fell, 1989) or the 15 June 2007 events affecting southern Germany (https://www.wetteronline.de/extremwetter/schwere-gewitter-und-starkregen-schaeden-durch-tief-quintus-2007-06-15-tq).

The third precipitation mode, explaining 12 % of the analysed days (Fig. 4), shows similarly to the first mode, an ECO, however, with an eastward shifting of the Azores ridge and the possibility of evolving to a Pivoting Cut-Off Low (PCO; Stucki et al., 2012). If the PCO finally realizes and reaches the Mediterranean it is accompanied by a cyclonic flow brining moisture originating at the Balkan region. This has been demonstrated to be the case for the second phase of the June 2013 flooding (Klemen et al., 2016). The fourth summer precipitation mode (Fig. 4), accounts for 11% of the considered episodes and represents situations of northeasterly development of the upper-level trough. The low pressure evolves into a CAT situation inducing a southwesterly moist inflow to the Alpine region (Stucki et al., 2012). The 08 July 2004 floods in Baden-Wuerttemberg (southwestern Germany; http://contourmap.internet-box.ch/app/okerbernhard/presse2.htm) are a good example

of such situation. The fifth precipitation mode, 8 % of the events, shows an STF pattern, similarly to the first winter precipitation mode (Fig. 3). Such a configuration was present during the Rhein-Necker flooding (western Germany) in June 2005 (https://www.rnz.de/nachrichten/metropolregion_artikel,-unwetter-folgen-in-mannheim-besonders-viele-
445 gebaeudeschaeden-durch-regen-_arid,482078.html).

4 Evaluation of ~~extreme~~ heavy precipitation

After identifying the synoptic situations responsible for heavy precipitation, we evaluate the RCM and CPM ~~Consortium for SMall Scale Modelling COSMO in Climate Mode (COSMO-CLM)~~ simulations ~~of the~~ between 2000 and 2015 ~~recent climate~~
(Tab. 2) in terms of probability, intensity, and detection capability ~~of extreme precipitation comparing the model results~~ against
450 observations.

Figure 5 shows empirical Probability Distribution Functions (PDFs) ~~box-and-whiskers distributions~~ of daily precipitation ~~larger than 1 mm d⁻¹~~ between 1971 and 2015 over SGer (Fig. 1). All datasets represent similar probabilities for precipitation intensities between 0 mm d^{-1} and 50 mm d^{-1}. The upper box in Fig. 5 shows a zoom-in for the lower intensities. Beyond 50 mm d^{-1} ~~RCM (blue) and~~ CPM (red) starts to diverge from RCM (blue) and the observations (HYRAS-5km in black and EOBS-
455 25km in grey). CPM (red) can represent daily grid point intensity up to 280 mm d^{-1}, whereas RCM (blue) can only attain 150 mmd-1. HYRAS-5km, for its part, reaches a maximum grid point intensity of 215 mmd-1 and E-OBS-25km reaches 180 mm d^{-1}. Figure 5 hence demonstrates that the coarser resolution data sets represent lower precipitation intensities. Finally, the differences in probability for intensities above 50 mm-d1 are to be noted. In this regard CPM shows the largest probabilities of representing heavy precipitation intensities (>120 mmd-1), ~~represent similar mean precipitation for the period (ca. 7 mm d⁻¹) but that CPM has a tail shifted towards the extremes. The 99-percentile for CPM (red, vertical bar) reaches 40 mm d⁻¹,~~
460 ~~whereas RCM (blue, vertical bars) is below 35 mm d⁻¹. The same occurs for maximum grid point precipitation. For CPM it reaches 360 mm d⁻¹ for CPM, whereas RCM has a 99-percentile of 250 mm d⁻¹.~~

The ability of CPM to represent larger precipitation rates agrees with previous literature (Ban et al., 2014; Prein et al., 2015; Fosser et al., 2014~~;~~), which has been related to the enhanced intensities over orographic terrain (Langhans et al., 2012; Vanden
465 Broucke et al., 2018; Ban et al., 2021). The comparison against HYRAS-5km (black), shows a good agreement by RCM and CPM for values between 1 mm d⁻¹ and 5~~1~~0 mm d⁻¹. However, CPM (red) overestimates ~~extreme~~ heavy precipitation for grid point maxima. This is a well-known deficit of CPM (Kendon et al., 2012; Berthou et al., 2018)~~)~~ in spite of its many advantages e.g., ~~This does not imply a worse performance by CPM for event representation since despite local grid point overestimations by CPM previous studies found robust~~ improvements in the representation of the diurnal cycle ~~, and the structure compared to~~
470 ~~RCM~~ (Kendon et al., 2012; Lin et al., 2018), or ~~. Furthermore, CPMs have shown systematically~~ better event representation ~~results when validating events, once aggregated in space and time~~ (Chan et al., 2012; Ban et al., 2018). ~~Finally, Fig. 5 also shows the agreement between HYRAS-5km and EOBS-25km with however a better capacity of HYRAS-5km to represent~~

~~large precipitation intensities, shown by the 99-percentile (vertical bar) and the grid point maxima (vertical line).~~ It should also be noted that even for grid resolutions down to 1 km the updrafts might not me simulated with the right intensity, which can help explain the overestimation of precipitation at these high resolutions (Vergara-Temprado et al., 2020). Also, the comparison against observations must be done carefully as heavy rain measurements might suffer from under catchment, which can reach even 58 % in the worst scenarios (Vergara-Temprado et al., 2020).

To further assess the performance of COSMO-CLM in representing precipitation extremes we analyse the detection ~~capabilities~~ capability of RCM (blue circles) and CPM (red dots) by means of a dot diagram, showing the 500 most severe events detected with the PSI in the period 1971-2015 over SGer (Fig. 6). The CPM dataset is extended to 1971 with the aid of the KLIWA-2.8km simulation that has a similar horizontal resolution (2.8 km) and is obtained using the same model (CCLM). However several inconsistencies exist between CPM and KLIWA-2.8 (refer to Sect. 2.2 for further details). We use HYRAS-5km (black circles and EOBS-25km (grey squares) as reference.

CPM (red dots) showed a higher spearman's rank correlation (0.48) than RCM (blue circles; 0.41) as shown in the legend of Fig. 6. The same applies to hit rate (number of hits divided by number of ocurrences) with values of 47.2 % for CPM and 45.88 % for RCM (not shown). The improvement shown by CPM with respect to RCM ~~is~~ shows ~~the~~some added value of high-resolution in ~~representing~~ detecting ~~extreme~~heavy precipitation events in a climatology. The rank correlations of both resolutions remain below 0.5 given the difficulty of exactly represent the same 500 events in a 44-year climatology representing 3% of all considered days. Figure 6 also show~~s~~ relevant periods of heavy precipitation clustering, e.g., spring-summer of 1971, winter 1989, the years 2000 to 2002 and autumn 2013. Regarding EOBS-25km (grey squares), it ~~shows~~has a rank correlation of 0.94 against HYRAS-5m ~~showing~~indicating a~~the~~ good accuracy ~~of~~for this product. Finally, the detection of cases in winter and summer in all datasets ~~indicates~~points at~~that~~ the PSI i~~a~~s a suitable method for extremes detection in all seasons.

5 Event scale evaluation

In the previous section, we assessed an overestimation of grid-point heavy precipitation for the convection-permitting simulation CPM, but a good performance in detecting severe precipitation events in a 44-year climatology. Here we evaluate the performance of CPM at the event scale. We focus on the period 2000-2015 and the ~~to warrant the consistency between the analysed simulations al forced with ERA-interim (Tab. 2). The~~ investigation area ~~region~~ is CPM~~ALP-3~~ (Fig. 1). ~~Furthermore, the availability of radiosonde observations for validation is larger after the year 2000 in the UWYO dataset in ALP-3, which further supports our selection of the investigation period.~~

Table 3 shows eight ~~subjectively~~ selected events ~~from~~ using the PSI ~~extremes detection~~, also included in the derivation of the synoptic weather types in Sect. 3. Table 3 includes information about the duration of the events, the observed total precipitation, maximum grid point intensities, percentage of affected area, i.e., percentage of grid points with precipitation over the 80th percentile, severity (PSI), and associated Weather Types (WT). The events showed a large severity (PSI) and were afterwards

short listed subjectively to include both winter and summer events. This is why some of them, e.g., 03-Nov-2002 or 08-Jul-2014, did not show heavy daily precipitation values but are however interesting for evaluating the model performance.

5.1 Precipitation

We evaluate the model performance focusing on two aspects of heavy precipitation, (1) the amount, calculated as aggregated precipitation in time and space, and (2) the structure, validated by means of the FSS metric (Sect. 2.3.3). For both metrics, we use MSWEP-11km (Tab. 1) as the observational reference, after coarse-graining all compared datasets to a common grid of 25 km. MSWEP-11km is used provided its large accuracy due to the inclusion of Rain Gauges (Beck et al., 2017) and since precipitation occurs to a large extent over the Mediterranean Sea, where HYRAS-5km and EOBS-25km have no coverage.

Table 4 shows the relative differences in precipitation amount aggregated in space and time between the model and observations as $RR_{rel.diff} = (MOD - OBS)/OBS$ in percent. CPM performed better than RCM in six out of the eight selected cases for precipitation amount. The largest improvement occurred for the 31-May-2013 event, which corresponds to the synoptic pattern S1 associated with the occurrence of ECOs and the advection of southwesterly moisture (Fig. 4) Using CPM brought generally larger precipitation rates, in agreement with the findings of Sect. 3, allowing for better scores of aggregated precipitation.

Regarding FSS, CPM performed well, in general terms, for 7 out of 8 events with FSS reaching values over 0.7. RCM, for its part, performed well for 5 out of 8 events (Tab. 4). The 31-May-2013 event is again an example of good performance by CPM, where the FSS scores reached 0.87 in CPM (0.26 in RCM). The main reason for this improvement was the ability of CPM to represent larger precipitation structures over the Alps in a better agreement with MSWEP-11km. The spatial distributions of precipitation are shown in Fig. S1 (supplementary material).

Only the event 08-Aug-2007, showed a bad performance by CPM, both for precipitation amount and structure. This event occurred under a S1 synoptic situation associated with an elongated troughs or cut-off lows (Fig. 4). The reason behind the bad performance in this case in CPM is the large underestimation of precipitation, which also hampers the structure representation.

Overall, these results showed that CPM brings added value in the representation of precipitation amount and structure compared to RCM. The advantage of CPM relies on the better location of orographic precipitation and the increased intensities brought by the more intense updrafts and larger number of cells triggered.

5.2 Humidity and temperature

In addition to precipitation errors, temperature and humidity biases could affect our interpretation of the model differences between RCM and CPM scale dependency. Here we validate specific humidity (hus) and temperature (ta) profiles from

~~COSMO-CLM~~RCM and CPM against radiosondes from the University of Wyoming (UWYO) and surface relative humidity (*hurs*) against EOBS-25km for the eight selected events (cf. Tab. 3).

535 Figure 7 shows the temporal Mean Bias (MB; thick line), the ~~spread~~ standard deviation of the differences (shaded area), and the Root Mean Square Errors (RMSE; dashed line) of specific humidity (Fig. 7a) and temperature (Fig.7b). The model output is interpolated to the location of eleven sounding stations where o ~~Only~~ ~~stations with~~ a height difference lower than 50 m between the station height and the model´s ~~RCM and CPM's model~~ orography is allowed~~are selected~~. This requirement is introduced to avoid including large humidity and temperature biases from differences in surface topography between the model

540 and the observations. We include all available soundings during the duration of the eight events (Tab. 3) in the calculation, with a temporal resolution between 6 h and 12 h.

Humidity is slightly overestimated by RCM throughout the whole profile and by CPM above 800 hPa (Fig. 7a). The overestimation by both models reaches 0.2 g kg^{-1} at 700 hPa. Below 800 hPa, CPM, reduces the mean bias reaching -0.1 g kg^{-1}, indicating a generally drier planetary boundary layer. RMSE values are very similar for both simulations being close to 1.5

545 g kg^{-1} below 700 hPa. These results are promising for ~~highlight the difficulties of the~~ COSMO-CLM ~~model~~ since neither RCM or CPM have an active data assimilation scheme and whence the model is exclusively constrained by the boundary conditions of the forcing data (ERA-interim). ~~in representing an accurate atmospheric humidity vertical gradient (Caldas-Alvarez and Khodayar, 2020; Caldas-Alvarez et al., 2021), which have been observed in other, similar, non-hydrostatic models (Risanto et al., 2019; Bastin et al., 2019).~~

550 Regarding temperature (Fig. 7b), COSMO-CLM shows a warm bias, ~~with mean bias~~ reaching 0.5°C ~~above~~ at the 925 hPa layer for both resolutions. RMSE (Fig. 7b, dashed line) is very similar between both simulations, ~~close~~ above ~~to~~ 2 °C, with a slight improvement by CPM (red). ~~The temporal averaged profiles of specific humidity and temperatures for these data sets can be found in Fig. S2 (supplementary material).~~

The humidity (Fig. 7.c) and temperature (Fig. 7.d) profiles show a wetter mid-troposphere (between 700 hPa and 925 hPa) in

555 RCM than in CPM and a very similar temperature profile between both simulations. CPM simulates slightly better the vertical humidity profile than RCM with a steeper humidity-height gradient. This was also observed in earlier studies with COSMO and COSMO-CLM (Caldas-Alvarez and Khodayar, 2020; Caldas-Alvarez et al., 2021). RCM compensates the deficiencies of parameterizing convection by simulating a wetter mid-troposphere, reducing the simulated dry-air entrainment ultimately increasing the total simulated precipitation. However, both simulations show a good performance considering the decadal

560 timescales

Provided the observations available below 925 hPa in the UWYO soundings were scarce, we employ the gridded EOBS-25km dataset (Tab. 1) to investigate the COSMO-CLM biases at the surface (Fig. 8). We represent the spatial distribution of temporal mean bias (colour shading) and the temporally-spatially averaged mean bias and RMSE of daily surface relative humidity. We

calculate relative humidity biases for this validation, given no surface specific humidity gridded observations with sufficient accuracy were available for our region and period of investigation.

COSMO-CLM underestimates surface relative humidity for both RCM (Fig. 8a) and CPM (Fig. 8b). This is especially so at the Po Valley (Italy) and the southern Italian Peninsula. However, CPM (Fig. 8b), slightly improves the surface relative humidity deficit at locations north of the Alps, e.g., northwestern France, the Czech Republic and western Austria. These corrections in the northwestern part of the simulation domain, reduce the temporal and spatial MB by 3%. However, provided the larger spatial variability of this variable in CPM, due to the better orography representation, the RMSE is worsened by 5 %.

The profile and surface humidity and temperature validation has shown that: a) COSMO-CLM shows performs well in simulating a the bias for the humidity and temperature lapse-rates, albeit small biases up to 0.2 g kg^{-1} in humidity and 0.5 °C (warm bias) in temperature exist; b) CPM simulates slightly better the vertical humidity profile with a steeper gradient than RCMgradient with height, simulating a drier than observations surface level and a wetter than observed atmosphere over 800 hPa both for RCM and CPM; b) COSMO-CLM presents a continuous warm bias, above 925 hPa; c) CPM reduces the positive surface relative humidity bias over locations north of the Alps, e.g., western France, the Czech Republic and eastern Austria.

6 Main modes of heavy precipitation variability in RCM and CPM Scale dependency of thermodynamic processes

We analyse the main modes of heavy precipitation in our simulations. We do this, applying PCA (Sect. 2.3.2) on heavy precipitation events detected in HYRAS-5km in the period 2000-2015. We obtain first the precipitation EOFs and represent their spatial distributions. We do this separately for winter (SONDJF) and summer (MAMJJA) events for both RCM and CPM, using only days above the percentile-90 of daily PSI values. In total, 290 events per season are considered to derive the EOF maps shown in Fig. 9 and Fig S.?? (Supplementary Material). For this analysis, we focus exclusively on precipitation EOFs with a similar structure between RCM and CPM, dismissing the remainder EOFs. This is done to ensure that we compare model differences in similarly simulated meteorological situations.

Figure 9 shows the four leading EOF maps for Winter events (panels a, c, e, and g) and the three leading modes in Summer (panels b, d, and f) as simulated by CPM. The corresponding figure for RCM can be found in the supplementary material (Fig. S??). After four EOFs in winter, the main modes of heavy precipitation variability start to differ considerably between RCM and CPM. These leading four winter EOFs explain 48% of the variability for RCM and 47% for CPM, being the first mode the most frequent one (22% of cases). For summer events the three leading modes of precipitation stand for 37 % of the situations in RCM and 33 % in CPM).

The first EOF for Winter events (Fig. 9a) is the mode associated with orographic precipitation over the Alps and the northern Apennines in the Genoa region. EOF-2 (Fig. 9c) shows precipitation either affecting continental Europe, north of the Alps (negative mode; brown) or affecting the Mediterranean, including the Italian and Balkan peninsulas with a marked orographic

595   signal (positive mode; green). EOF-3 (Fig. 9e) combines precipitation over northern Europe with Mediterranean precipitation in its positive mode (green). The negative mode (brown) affects the southern Mediterranean basin between Italy and France as well as the southern and Maritime Alps. EOF-4 finally shows a positive mode associated with Precipitation over the Gulf of Lyons, the Balearic Sea and the Pyrenes (green), and a negative mode affecting northeastern Italy (brown). Both situations of heavy precipitation in the Mediterranean have been studied in detail in the HyMeX project (Khodayar et al., 2021).

600   The first EOF for summer events (Fig. 9b) is associated with orographic precipitation over the Alpine region, similarly to winter EOF-1, albeit affecting parts of northern Europe, where convection can trigger more easily during the summer months. EOF-2 (Fig. 9d) shows a similar pattern to winter EOF-4 (Fig. 9g) and EOF-3 shows a pattern similar to Winter EOF-2 (Fig. 9c).

7 Model differences between RCM and CPM using composites

605   To further analyse model differences between RCM and CPM, we derive composites of model variables from each EOFs in Fig. 9. We focus on model variables influencing the simulation of heavy precipitation simulation e.g., Integrated Water Vapour (IWV), Convective Available Potential Energy (CAPE), soil-atmosphere heat fluxes, etc. To derive the composites, we select the days where daily precipitation showed the largest resemblance to the positive and negative modes of the precipitation EOFs. In other words, we select the days showing the largest positive (negative) correlations to each precipitation EOF. This

610   is done separately for RCM and CPM selecting the days with positive and negative correlations larger than one standard deviation of the whole set. This leads to composites of ca. 30 days. We average in time the spatial distribution of the selected days and obtain maps of the differences between RCM and CPM as in Fig. 10. For heavy precipitation differences, we work with composites of the days assigned to each EOF, whereas for the other model variables we use the day prior to heavy precipitation. This done to study the model differences in the pre-conditioning of the event.

7.1 Heavy precipitation

615   The composites show relevant differences in precipitation amount (up to 15 mm h^{-1}) between RCM and CPM throughout the complete greater Alpine domain, irrespective of the simulation and meteorological situation. Spatially averaged, both RCM and CPM can represent larger precipitation than their counterpart, however, in summer, CPM represents larger precipitation at the mountain tops e.g., the Alps, the Apennines. This is so for all analysed EOFs and both positive and negative correlations

620   of the principal components. For illustration, Fig. 10a shows the composite differences of the negative principal components of EOF-2 in Winter. Differences up to 6 mm h^{-1} are located east of the Spanish coast (RCM, blue) over the Apennines (Italy) and over the eastern and the Dinaric Alps (CPM, red). Spatially averaged, RCM simulates larger precipitation (0.21 mm h^{-1}), but this varies between EOFs. Fig. 10b shows the positive principal components of EOF-3 in summer, where again, CPM simulates larger precipitation than RCM over the Apennines (Italy), the Dinaric Alps (Balkans), and to a lower extent over the

625 western Alps (Switzerland) and the Central Massive (France). All remainder composites are included in the supplementary material.

These results highlight that RCM and CPM can simulate comparable precipitation amounts in the timely averages of daily precipitation (for the investigated EOFs). Regarding the larger precipitation amounts simulated by CPM over the mountain ranges, a plausible explanation is be the intensification of vertical winds observed in previous studies comparing horizontal
630 resolutions (e.g., Langhans et al., 2012; Barthlott and Hoose, 2015; Vergara-Temprado et al., 2020). Another explanation is provided by Vergara-Temprado et al., (2020) addressing that the "increase in precipitation with resolution could be happening as smaller grid boxes are easier to reach saturation". However, the presented analysis does not allow splitting the contributions from resolution increase from other factors, e.g., changes in the physics or physical parameterizations (see Sect. 2.2).

7.2 Integrated Water Vapour (IWV) and Equivalent Potential Temperature at 850hPa (θ_e^{850})

Two variables typically regarded as precursors of heavy precipitation are IWV and θ_e^{850} (Doswell et al., 1996; Stucki et al., 2016). The differences of the composites show larger IWV in RCM compared to CPM throughout the greater Alpine region. This applies to all analysed EOFs and their respective positive and negative components. The IWV differences can be as large as 2 mm and take place especially over the Mediterranean Sea and the Po Valley. Regarding θ_e^{850}, we observe an analogue
640 overestimation by RCM compared to CPM that can be as large as 4 K. Atmospheric water vapour is the main precursor of the θ_e^{850} differences as RCM is wetter than CPM in the 850 hPa level (not shown). For illustration Fig. 11 shows the composite differences of IWV (colour shading) and θ_e^{850} (contours) for the same principal components as Fig. 10. The composites show IWV differences up to 1 mm over the Mediterranean Sea and up to 2 K for θ_e^{850}. Likewise, the negative principal components of EOF-3 show IWV differences up to 3 mm over France and 3 K differences in θ_e^{850} by RCM (blue). The remainder
645 composites can be found in the supplementary material.

7.3 Soil-Atmosphere interactions

The surface conditions play a relevant role for convection initiation, specially under weakly forced environments (Keil et al., 2020) and are thus worth investigating.
In the pre-conditioning of winter events, CPM simulates larger outbound latent heat fluxes than RCM over land (by about 15
650 W m^{-2}). The opposite occurs over the Mediterranean. Over large water bodies, RCM simulates about 30 W m^{-2} more than CPM. This holds for all composites derived from the EOFs presented in Sect. 6 (Fig. 9). The explanation is that the signal is already present in the seasonal means (see Fig, ?? in the SM) and hence is not characteristic of heavy precipitation exclusively. For illustration, Fig. 12a shows the composite differences of the negative principal components of EOF-3 (Fig. 9e). CPM exceeds RCM in 15 W m-2 over land, but RCM shows ca. 15 Wm-2 more latent heat emissions than RCM. The remainder
655 composites can be found in the SM.

Sensible heat fluxes have shown no clear differences between RCM and CPM over the Mediterranean Sea. Over land, during winter, we cannot assert the magnitude of these differences since the soil temperatures are too low to show any outbound heat emissions. Figure 12b illustrates these results. Where differences over the sea ar close to zero and green colours denote no positive outbound heat emissions over land.

660 Specific humidity and temperature at the surface are influenced by differences in the simulation of latent heat fluxes in RCM (Figs. 12c and 12d). Provided the larger outbound latent heat flux over land in CPM, the regions north of the Italian Peninsula show generally larger specific humidity in CPM than RCM (by about 1 g kg^{-1}). On the contrary, over the Sea RCM is wetter than CPM in all analysed EOFs (by about 1 g kg^{-1}). Over Italy, the surface specific humidity differences are also larger in RCM influenced by the sea southerly winds, which inflow maritime air masses in RCM than CPM. Regarding temperature,

665 RCM simulates a warmer surface level (land and sea) of variable magnitude between 1 and 2 °C. This applies for all composites except one. This signal is also present in the seasonal means already and cannot be considered exclusive of heavy precipitation situations (Fig. ?? of the SM).

Because CAPE is calculated in COSMO-CLM from the lowest 50 mb layer, differences in humidity representation can influence the representation of CAPE. However, for winter events the RCM vs CPM show no systematic differences due to

670 the lower CAPE of this season. This can be seen in Fig. 12e and the remaining composite plots in the SM.

Finally, the higher temperatures over land and sea in RCM induce larger outbound long wave surface radiation than CPM, by ca. 10 W m^{-2} (Fig. 12f). This, likewise, surface temperate applies to all analysed composites except one.

Regarding Summer events, CPM again shows larger emissions of latent heat flux over land than RCM (ca. 15 W m^{-2}) but now these differences are limited to the Alps and northern Europe (Fig. 13a). For its part, RCM now shows larger latent heat

675 emission over the Sea but also throughout the Italian peninsula up to the Po Valley. This is the case for all summer composites except one (see SM).

Sensible heat fluxes during summer events are larger in RCM than in CPM over land and Sea up to 20 W m^{-2}, although these differences tend to be smaller on coastal areas and the Po valley (Fig. 13b). This applies to all analysed EOFs.

The previous results must be interpreted with caution. First, the north-south signal of latent heat flux differences is already

680 present in the seasonal means (see Fig. ?? in the SM), and hence cannot be understood as characteristic of heavy precipitation situations exclusively. Second, the partition between latent and sensible heat fluxes is governed, although not exclusively, by the water content in the upper soil layers. Unfortunately, the RCM and CPM simulations used in this study bear a different integration of volumetric water soil and cannot be compared. Finally, because we obtain composites from the days prior to heavy precipitation, our results could be affected by earlier precipitation. In other words, if the events were preceded by some

685 precipitation in either RCM or CPM, the upper soil levels will inevitably show a soil wetter than its counterpart.

For surface specific humidity RCM represents larger values than CPM over the Mediterranean as well as the Po Valley and the Italian peninsula (ca. 1.2 g kg^{-1}). Over northern Europe CPM tends to simulate larger specific humidity although not as systematically as for the winter composites. Figure 13c shows the CPM (red) and RCM (blue) specific humidity differences over northern Europe and the Mediterranean region respectively.

690 Regarding temperature, RCM represents ca. 1.3 °C more than CPM throughout the whole domain. However, differences are weaker over the Mediterranean Sea and the Po Valley, and one composite even shows a temperature excess for CPM (EOF-2). This is shown in Fig. 13d.

The weaker temperature differences between RCM and CPM over the Po Valley agree with previous findings assessed in Sangelantoni et al., (2022). The authors of this study, comparing an ensemble of CPM and RCM simulations, observed that 695 CPM amplifies the drier-warmer conditions during heat waves with respect to the RCM ensemble. Furthermore, they assessed that "latent heat flux modulation tends to characterize not only HW events but also the whole summer season. Although our composites do not show such a clear temperature overestimation by CPM over the Po Valley, they show a tendency that warmer conditions can be simulated by CPM over this area.

Regarding CAPE, CPM shows larger values over land than RCM, whereas RCM simulates larger CAPE over the Sea (Fig. 700 13e). A plausible explanation are the surface specific humidity differences assessed before that can influence the instability of the lowest air masses, used in the same calculation. Finally, the outbound long wave radiation as it was the case for winter, shows the same sign of differences as surface temperature, with a general overestimation by RCM, compared to CPM (Fig. 13f).

We analyse the scale dependency of model variables related to thermodynamical processes of heavy precipitation in the 705 investigation area ALP-3. To this end, we use PCA as described in Sect. 2.3.2 with daily precipitation in the period 2000-2015 from RCM and CPM. We obtain the precipitation EOFs separately for winter (SONDJF) and summer (MAMJJA) for both resolutions. We derive composites of model variables related to thermodynamic precipitation processes, e.g. moisture transport, instability, or soil atmosphere fluxes and we select precipitation days of each EOF with PC values larger than one standard deviation of the time series. This implies using data of about 400 days out of a time series of 2900 days associated to 710 each EOFs. Then the timely averages for each variable and EOF from RCM are subtracted to the temporal averages of CPM for the days prior to heavy precipitation days to derive composites of the resolution differences. Following Ulbrich et al., (1999), we use composites of timely averages, to avoid assuming linearity between the precipitation PCs and the variables' temporal evolution, as is the case when the Pearson correlation is calculated.

To study the scale dependency of thermodynamic variables, we focus exclusively on precipitation EOFs with a similar 715 structure between RCM and CPM. This is done to ensure comparability between both resolutions. Being precipitation a highly variable quantity, winter and summer EOFs start to differ considerably after the fourth EOF for winter and the third EOF for summer. We do not consider the subsequent principal components. The leading four EOFs for winter explain 46% of the variability for the RCM and 42% for the CPM simulation. The first three EOFs for summer, for its part, explaining 39% of the situations in RCM and 33% in CPM). Here EOF-1 is presented for illustration (Fig. 9) but the remainder analysed EOFs can 720 be found in the supplementary material (Figs. S3, S4, and S5).

The first precipitation EOF has a very similar pattern between RCM and CPM (Fig. 9). For the winter season, both data sets (Figs. 9.a and 9.c) are dominated by orographic precipitation, over the Pyrenees (France), Corsica and the Central Massive

(France), the Alps (Germany), and the Apennines (Italy). The differences of the composites (Fig. 9.e), clearly show larger precipitation in CPM (red) than in RCM (blue) over the mountain systems, as expected from the intensification of vertical winds and more frequent triggering of convective cells (Langhans et al., 2012; Barthlott and Hoose, 2015). For lower terrain, CPM (red) only shows more precipitation north of the Alps than RCM. The opposite occurs for RCM (blue), showing larger precipitation over the Mediterranean Sea and the Po Valley (Italy). Spatially averaged, the CPM composites showed -0.14 mm h^{-1} less than RCM (Fig. 9e). Chan et al., (2012) pointed at these differences between low and high terrain, arguing a lower skill of convection permitting models for lowlands.

For summer (Figs. 9b, 9d, 9f), a similar scale-dependency is found, with orographic precipitation dominating the total amount in RCM and CPM. The composite differences (Fig. 9f) show larger precipitation by CPM over the mountain tops. At low altitude terrain, the summer composites show larger precipitation by RCM towards the northern Alpine region (Austria, southern Germany; Fig. 9b). The spatial average of precipitation differences for this season is -0.12 mm h^{-1}, again with CPM showing larger precipitation than RCM.

The findings based on the main modes of precipitation variance, for which EOF-1 is shown as an example, can be summarized as follows: (a) CPM displays larger precipitation than RCM over the mountains for all assessed EOFs and winter and summer seasons. RThis points at resolution differences in dynamic processes, e.g., increased vertical wind speeds, larger triggering of convective cells (Langhans et al., 2012; Barthlott and Hoose, 2015) could play an important role in these differences, invigorating the precipitating systems for this mode ; to be the main precursors of the differences; especially since EOF 1 has a marked orographic patternis the most frequent precipitation mode. (b) Over lowlands and the Mediterranean, the dynamical factor alone cannot explain the precipitation differences.

To understand precipitation differences at low terrain due to model resolution, Fig. 10 shows composite differences for model variables related to thermodynamic precipitation processes, relative to EOF-1. For the calculation of the composite differences, we use the day prior to the selected precipitation days to study the preconditioning pre-existing conditions of the precipitation events environment.

Figure 10.a shows winter differences in specific humidity at the surface (*huss*; colour shading), and precipitable water vapour (*prw*; contours). The surface specific humidity differences show a north-south gradient, changing from higher surface humidity in CPM north of the Alps (red), up to 0.4 mm, to higher humidity in RCM (blue) over the Alps, Italy, and the Mediterranean Sea (0.8 mm). Regarding precipitable water vapour, RCM (positive contours) represents systematically a wetter atmosphere, especially over Italy and the Mediterranean Sea with differences up to 1 mm in compared to CPM. This holds for all four analysed winter EOFs. Figure 10.c shows composite differences of CAPE (colour shading) and Equivalent Potential Temperature at 850 hPa (θ_e^{850}; isolines). CAPE is larger over the Mediterranean for RCM (blue) up to 80 J Kg^{-1} more, but larger for CPM (red) over western France. θ_e^{850} is 1 K larger in RCM over the Adriatic Sea and eastern Italy. This is probably

due to the larger moisture amount in RCM at the lower mid-troposphere. Fig. 10.e, shows differences in outbound sensible heat flux ($hfss$; colours) where green colours denote grid points in RCM or CPM with no outbound fluxes of sensible heat. The contours in Fig. 10c represent surface temperature at 2 m (tas). Due to the colder soil conditions in winter, RCM and CPM show predominantly a surface-directed flux of sensible heat over land (green colours). Over the Sea, the atmosphere-directed surface flux of sensible heat is dominated by RCM with an excess up to 10 W m^{-2}. Surface temperature is larger by 1 K in RCM compared to CPM over land with no differences over the Sea. Finally, Fig. 10.g shows differences in outbound latent heat flux ($hfls$, colour shading) and wind speeds at 10 m height ($sfcwind$; contours). Differences in atmosphere-directed latent heat fluxes show a marked land-sea contrast with larger emissions over land for CPM (red) but larger emissions over the Sea for RCM (blue). This agrees well with the differences observed in outward surface sensible heat flux which show an opposite sign to keep a similar Bowen's ratio over land. RCM shows about 0.2 m s^{-1} higher 10m wind speeds at the surface over the Sea and the Italian peninsula, whereas CPM shows higher winds over the Alps. In the northern part of the domain, the differences in the wind speed are negligible.

Figure 10.b shows the results for summer EOF-1 composite differences. Analogously to winter, RCM (blue) shows larger surface-specific humidity, up to 1 g kg^{-1} more than CPM (red) which affect the whole investigation domain except northern Europe (Fig. 10.b). Precipitable water vapour is analogously larger in RCM than in CPM with differences up to 1.5 mm in the complete domain. These differences are larger in summer composites than in winter because of the larger water capacity of warmer air masses. Figure 10.d shows larger CAPE by RCM (blue) along the Adriatic, the western Mediterranean and the Po Valley (Italy), whereas CPM (red) represents larger CAPE north of the Alps and the Balkans with no differences over the Apennines (Italy). On the contrary, differences in θ_e^{850} (Fig. 10.d, contours), show an excess in RCM (positive contours) over the whole domain, up to 3 K. Figure 10.f shows that RCM represents larger outbound surface sensible heat fluxes over all land areas up to 30 Wm^{-2} (blue colours), with no remarkable differences over the Sea, similarly to winter EOF-1. For surface temperature (contours), the warmer surface level in RCM due to enhanced emission of sensible heat occurs likewise in summer, although with larger differences (1.5 K over western France). Finally, Fig. 10.h, shows larger outbound latent heat fluxes (colour shading) in RCM (blue) over the Sea but larger emissions of latent heat in CPM (red) over land, with the only exception of the Po Valley. Wind speed at the surface (contours in Fig. 10.h) is larger in RCM than in CPM over northern France, but the opposite occurs, over the Alps and the northwestern Part of the Mediterranean (south to France). Over the Apennines, the differences are negligible.

The analysis of the composites showed new insights on how precipitation differences relate to the scale dependency of thermodynamic processes. We presented the results of EOF-1 for illustration (Fig. 10) but the remainder EOFs are included in the supplementary material (Figs. S6, S7, and S8). Our findings indicate for all EOFs in winter and summer that: a) precipitation differences due to resolution at lowlands are related to the differences of the thermodynamic variables analysed here b) the variable whose scale-dependency showed the largest impact on precipitation differences at lowlands was surface specific humidity. Larger surface humidity in RCM or CPM in the day prior to the event, determined whether RCM or CPM

represented larger precipitation; c) precipitation differences for EOF-3 and EOF-4 in Winter and EOF-1 in Summer could not be explained through resolution differences in surface specific humidity. For those EOFs, RCM represented larger precipitation, if the events were preconditioned conditioned by very large θ_e^{850} differences (3 K or more) as is the case for EOF-4 in winter and EOF-1 in summer. On the contrary, , whereas CPM simulated larger precipitation where the preconditions pre-existing conditions showed larger CAPE and stronger surface winds, e.g., in CPM as in EOF-3 in winter; d) generally, CPM represented a wetter surface north of the Alps and RCM represented a wetter surface over the Mediterranean Sea and the Italian Peninsula; e) the surface specific humidity differences can be explained through differenctes latent heat fluxes between RCM and CPM, where RCM evaporates more moisture over the Sea and CPM over land. Provided the predominant southwesterly to southeasterly flow in the Mediterranean region transporting moist air masses (Toreti et al., 2010), the Italian peninsula predominantly showed a wetter low level in RCM compared to CPM; f) outbound sensible heat fluxes and surface temperature over land, were systematically larger in RCM compared to CPM; f) CAPE was systematically larger in CPM over land and surface winds were stronger in CPM over the Sea and the Alps.

7 8 Conclusions

The recent advancements in computational capacity have fostered the use of Convection Permitting Modelling (CPM; horizontal resolution below ca. 4 km) for decadal atmospheric simulations. This has been of pivotal relevance for the understanding and simulation of heavy precipitation events with large impact at these timescales. Despite the improvements assessed for the simulation of this atmospheric hazard, not all implications of reaching CPM resolutions are known and further research is needed to evaluate and understand how CPM simulates heavy precipitation and its associated processes. In this study we have evaluated and comparedd decadal reanalysis-driven simulations of the greater Alpine area in a Rnegional Climate Model (-RCM) set-up of 25 km and a CPM set-up of 3 km in the period 2000-2015. The main results are described below.(parameterized deep convection at 25 km) and a CPM (explicitly resolved deep convection at 3 km) setups, to assess the scale-dependency of thermodynamical processes influencing extreme precipitation. The main results are:

a) We adapted the The implemented Precipitation Severity Index (PSI), an index used for heavy event ranking, to include a persistence parameter and showed that it is a useful index to detect severe precipitation events in decadal datasets. The main advantage is its flexibility to account for precipitation persistence but also to allow for definition of an intensity threshold. Including these two parameters favours the ranking of longer-lasted and rarer events whereas setting them to zero leads to a normal spatial averaging of daily precipitation. considering heavy grid point precipitation intensities, with large spatial coverage and persistence is a suitable index for extremes detection both for summer and winter periods.

b) Principal component analysis showed that Wwinter heavy precipitation events detected from daily observations in during the 1971-2015 period in the greater Alpine area occur either under stationary front situations with northerly low pressure

descending to central and Southern Europe (EOF 1) or under strong north-south gradients of the 500 hPa geopotential height with a strong zonal flow (EOFs 2, 3, and 4). Four principal weather types sufficed to explain the major part of the natural variability of winter cases.

c) Using daily precipitation data we find that sSummer events are associated to either frontal convection on the western sector of elongated upper-level troughs and evolved cut-off lows (EOFs 1, 3 and 4), or due to winter-like synoptic patterns of stationary fronts over central Europe or strong zonal flows (EOFs 2 and 5). Five PCs wereare enoughsufficient to explain the major part of the natural variability of summer cases.

d) The validation of the RCM and CPM against observations showed that CPM set uprepresents shows larger precipitation intensities, a better rank correlation, better hit rates for extremes detection, and a better representation of precipitation amount and structure for the selected HPEs, compared to RCM. However, CPM overestimates grid point intensity compared to observations, especially at high altitudes such as the Alps or the Apennines (also observed in Langhans et al., 2012, and Ban et al., 2020). However the observations over mountainous terrain might as well be strongly underrepresented due to a lack of measurements to account for the high spatial variability.

Principal component analysis revealed that the leading modes of heavy precipitation events started to differ substantially between RCM and CPM after the fourth leading mode in winter (47% of cases) and the third leading mode in summer (33 % of cases). This implies that more than half of severe precipitation events are represented differently in RCM and CPM and thus the choice of modelling approach is crucial, especially for summer cases. Composite maps derived from the leading modes showed that daily precipitation differences between RCM and CPM can be as large as 200 m d^{-1} for both simulations indistinctively, although CPM tends to simulate larger precipitation than RCM over the mountain systems.

Regarding other model variables, the composite analysis showed that RCM represents larger Integrated Water Vapour than CPM for most of the analysed precipitation modes. This is especially so over the Mediterranean Sea and the Italian Peninsula for summer events. The moisture excess in RCM comes from an intensified latent heat flux emission over the Sea and the Italian peninsula (especially in Summer) and a more humid lower free troposphere throughout the whole year. This was validated for 8 selected reprecipitation events against radiosondes. As a result, Equivalent Potential Temperature at the 850 hPa level was also systematically larger in RCM than in CPM (up to 3 K).

Latent heat flux in CPM was larger than in RCM (up to 15 W m^{-2}). Over the Sea, the opposite occurs, and RCM overestimates latent heat flux compared to CPM (30 W m^{-2} more). The consequence is that CPM simulates larger specific humidity over land areas north of the Alps (1 g kg^{-1}) but RCM simulates more specific humidity over the Sea and Italy. The wind transports the moisture excess in RCM toward the coast. Regarding differences in surface temperature, RCM showed a systematically colder surface level (by about 1.5 °C). This, in turn, brought larger emissions of outbound long wave radiation in RCM compared to CPM.

For Summer events, the same model differences take place. Although, the larger latent heat fluxes simulated by CPM over land are now restricted to land areas north of the Alps. Surface sensible heat fluxes, on the contrary, are larger over land in RCM than in CPM (up to 20 W m^{-2} more), although these differences are weaker over the Po Valley. The consequence is an overestimation of surface specific humidity by CPM north of the Alps and by RCM over the Mediterranean and Italy compared to their counterpart. Surface temperature is higher in RCM than in CPM north of the Alps, but the differences are weaker over the Po Valley and Italy. Due to the larger specific humidity north of the Alps in CPM CAPE is also larger for this simulation over land areas than in RCM, whereas outbound long wave radiation is larger in RCM, linked to the warmer surface level in this simulation.

e) The scale-dependent precipitation differences over elevated terrain are explained by differences in the dynamical factors of deep convection, i.e., intensification of the updraughts, and larger triggering of convective cells in CPMs assessed in previous studies (Langhans et al., 2012; Vanden Broucke et al., 2018; Heim et al.2020).

f) Conversely, precipitation differences over low terrain are mostly related to the scale dependency of thermodynamic variables. Among the analysed variables, surface specific humidity, showed the largest impact. An excess for this variable up to 1 g kg^{-1} on the day prior to precipitation in RCM (CPM) induced larger precipitation totals at low altitudes in RCM (CPM). Since RCM showed generally larger surface humidity over the Mediterranean and the Italian peninsula, and CPM showed larger surface moisture north of the Alps, precipitation differences at low elevations showed generally a north-to-south spatial distribution.

g) The larger surface specific humidity in RCM over the Mediterranean and the Italian Peninsula, and the larger surface humidity in CPM north of the Alps are due to resolution differences in outbound latent fluxes from the soil to the atmosphere. RCM showed an intensified emission of latent heat over the Mediterranean Sea (25 W m^{-2}), whereas CPM, showed larger latent heat emission over land (15 W m^{-2}). The southerly winds, over the Mediterranean and Adriatic Seas induced an inland transport of surface atmospheric moisture through the Po valley and the Italian peninsula. These resolution differences in latent heat fluxes are responsible for the slight improvement in the simulation of surface relative humidity assessed for CPM (3 % less mean bias), north of the Alps.

h) Contrary to latent heat, RCM emits more sensible heat fluxes over land than CPM, up to 40 W m^{-2}. This induces larger surface temperatures in RCM up to 1.5 °C compared to CPM. The differences over the Sea are negligible.

Our study presents new insights on the scale-dependency of precipitation thermodynamic processes. However, new research questions remain open that should be subject to further investigation. The underestimation of moisture at the surface at both resolutions (RCM and CPM), which is slightly improved north of the Alps in CPM must be assessed further. More knowledge is needed as to whether other established regional climate models present similar shortcomings. Furthermore, this work points at the scale-dependency of surface humidity as a precursor of precipitation differences over low terrain. However, more research is required as this general response to surface humidity differences could not be asserted for all analysed precipitation

modes, namely EOF 3 and EOF 4 in Winter and EOF 1 in Summer. For these EOFs, the scale dependency of CAPE, θ_e^{850} and surface wind speed played a larger role. In-depth analysis for individual HPEs is encouraged to assess these model responses. Finally, our work highlights the existent dichotomy between low vs. high terrain and dynamic vs. thermodynamic factors of the scale dependency representation of extreme precipitation. This aspect should be considered in future scale-dependency studies of the greater Alpine area and other orographically complex areas.

Our study has some limitations that need to be briefly addressed. First, we only assess one regional climate model and hence our results cannot be generalized to other RCMs. Second, as is common in heavy precipitation studies the under-catchment problem might be present in the observations used for validation (Vergarara-Temprado et al., 2020). Third, we would like to point out that our study compares two completely different simulations and that the differences observed are not just due to the use of a different horizontal resolution (25km vs 3km). Different physical schemes are used as well as different boundary data. Finally, we would like to emphasize that some of the model differences, are already present in the seasonal means, especially for soil-atmosphere interactions. This means that they cannot be considered exclusive of heavy precipitation environments. However, they are valuable information for other modellers in the community as they shed light on COSMO-CLM intrinsic biases. For instance, the fact that CPM represents larger temperature at the Po Valley in the pre-conditioning of precipitation adds to the findings of Sangelantoni et al., (2022) where CPM shows drier-warmer conditions over the same area.

Besides, we performed precipitation and humidity validations only for eight selected case studies, an insufficient number to derive statistically robust conclusions for the climatology. However, this evaluation provide a first estimation of the overall model's performance. Finally, the combination of two different simulations (KLIWA 2.8 km and ALP 3 from the FPS-Convection project) to build the CPM are not identical (Tab.2). We decided nevertheless to combine both simulations to profit from a larger time span, that enables studies on climatic scales.

Notwithstanding these limitations, our study provides evidence of the added value of using CPM for climate studies and the differences that exist with respect to RCM that must be considered when employing one approach or the other. Despite the assessed positive model bias for mountain heavy precipitation, the good results in the event validation and detection capabilities in the climatology, as well as the improved description of the physics, emphasize their applicability in both climate and impact studies. Examples of endeavours where high-resolution climate data bring added value are, for instance, the downscaling of climate change projections (Pichelli et al., 2021), the development of decision-relevant strategies for Climate Change adaptation (BMBF-RegiKlim) or their use in forestry or hydrology applications interesting for the scientific community and stakeholders.
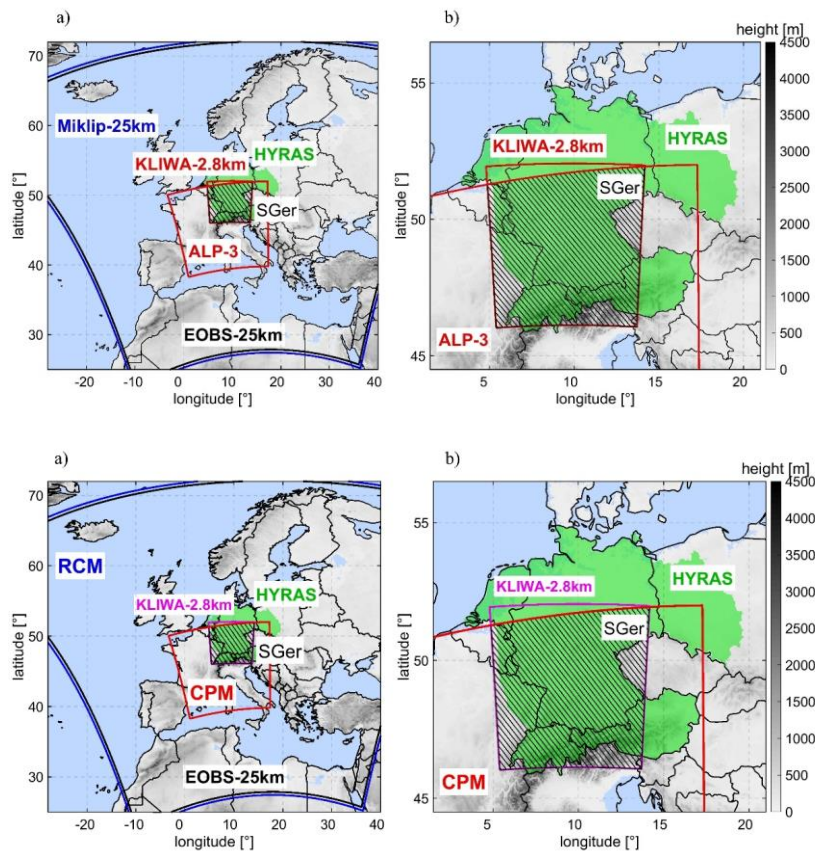
Figure 1. a) Simulation, and observation domains of for RCM (25km; Miklip-25km (blue), CPM (KLIWA-2.83 km; red) (red), KILA-2.8km (magenta); ALP-3 (red), and observations' coverage of HYRAS-5km (green), and EOBS-25km (black). The two investigation domains of this study are Southern Germany (SGer; dashed box), and the CPMALP-3 domain.

915

920

a)

	$fldsum$	PSI ($RR_{80_{ij}}$, $d=0$)	PSI ($RR_{80_{ij}}$, $d=2$)	PSI ($RR_{95_{ij}}$, $d=2$)
Rank Corr.	1.00	0.97	0.96	0.86
1	07-Aug-1978	07-Aug-1978	22-Oct-1986	22-Oct-1986
2	14-Feb-1990	14-Feb-1990	15-Feb-1990	14-Feb-1990
3	20-Nov-2015	20-Dec-1993	14-Feb-1990	20-Dec-1993
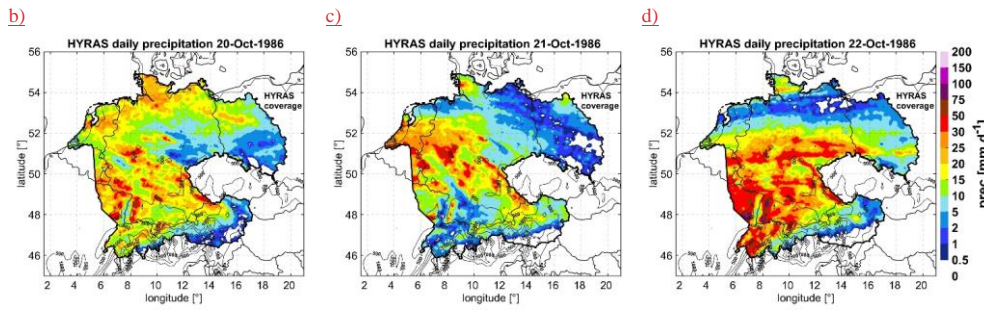
Figure 2. (a) Rank correlations between $fldsum$ and different configurations of the PSI daily values in the period 1971-2015 over SGer obtained with HYRAS-5km. The top three events of the period are shown for each index. (b), (c), and (d) show spatial distributions of daily precipitation measured by HYRAS-km on the 20, 21 and 22 October 1986.
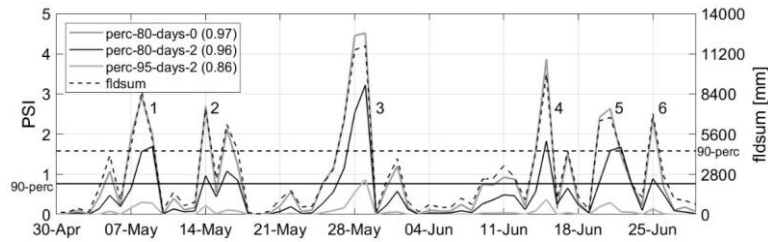
Figure 2. Daily PSI (left axis) and field sums (fldsum; right axis) over the SGer investigation area between 30 April and 29 June 2007 based on HYRAS-5km. Different settings of the percentile ($RR_{perc_{ij}}$) and persistence (d) parameters in the PSI calculation (Eq. 1) are tested. Namely, the 80th percentile and a persistence of 0 days (perc-80-days-0; dark grey), an 80th percentile and a persistence of 2 days (perc-80-days-2; black), and a 95th percentile and a persistence of 2 days (perc-95-days-2; light grey). For comparison, fldsum is shown (dashed black line). The legend shows in brackets the Spearman's rank correlation of the different PSI calculations with fldsum. The 90th percentile values of the PSI (left) and fldsum (right) for the whole 1971-2015 climatology are shown by horizontal lines. Six HPEs denoted by numbers take place during the shown period, the 7-11 May event over northern Germany and the Alps (1), the 14-17 event affecting northern Poland and the Alps (2), the 27-29 May convective events over central Germany and the northern Alps (3), the 15 Jun event over central Germany (4), the 20-21 June over northern Germany and eastern Poland (5), and the 25-Jun Alpine event (6), see Schaefer et al., (2007).
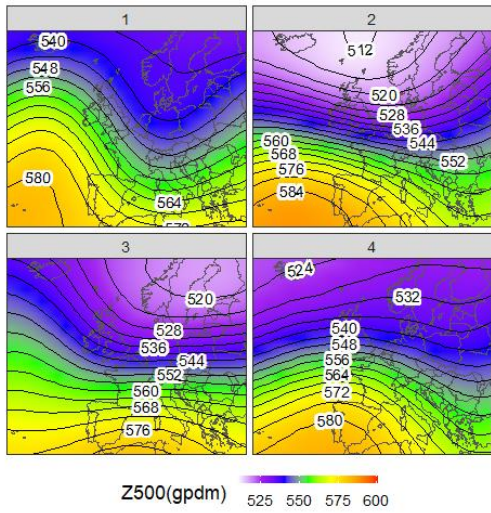
Figure 3. Synoptic ~~classification~~ weather patterns based on Principal Component Analyses for the 98-percentile most severe precipitation cases in winter (SONDJF) of the 1971-2015 period, detected with the PSI. ~~The selection of the number of PCs is based on parallel analyses and randomization of the distribution eigenvalues (λ; Peres-Neto et al., 2005).~~ The spatial distributions show 500 hPa geopotential height in geopotential decameters (gpdm) obtained from RCM. The analysis has been performed with the SynoptReg R package (M. Lemus-Canovas et al., 2019).
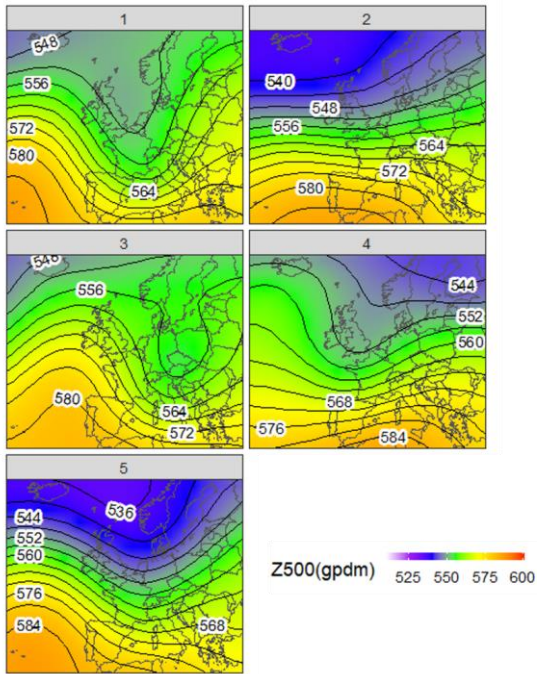
Figure 4. As Fig. 3 for summer extreme precipitation days (MAMJJA). ~~5 PCs are discernible from random noise.~~
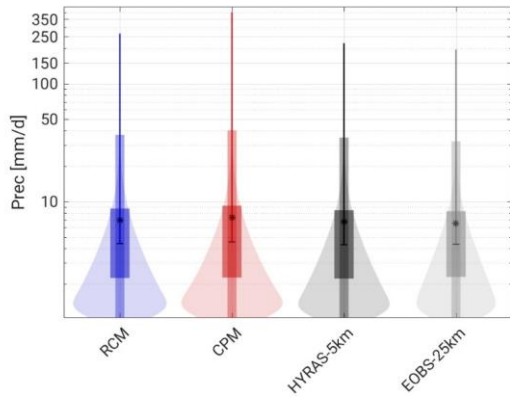
950

955

Figure 5. Empirical Probability Distribution Functions (PDF) of daily precipitation over SGer in the period 2000-2015 from HYRAS-5km (black), EOBS-25km (grey), RCM (blue), CPM (red). The lowest precipitation rates are shown in the upper-right corner subpanel.
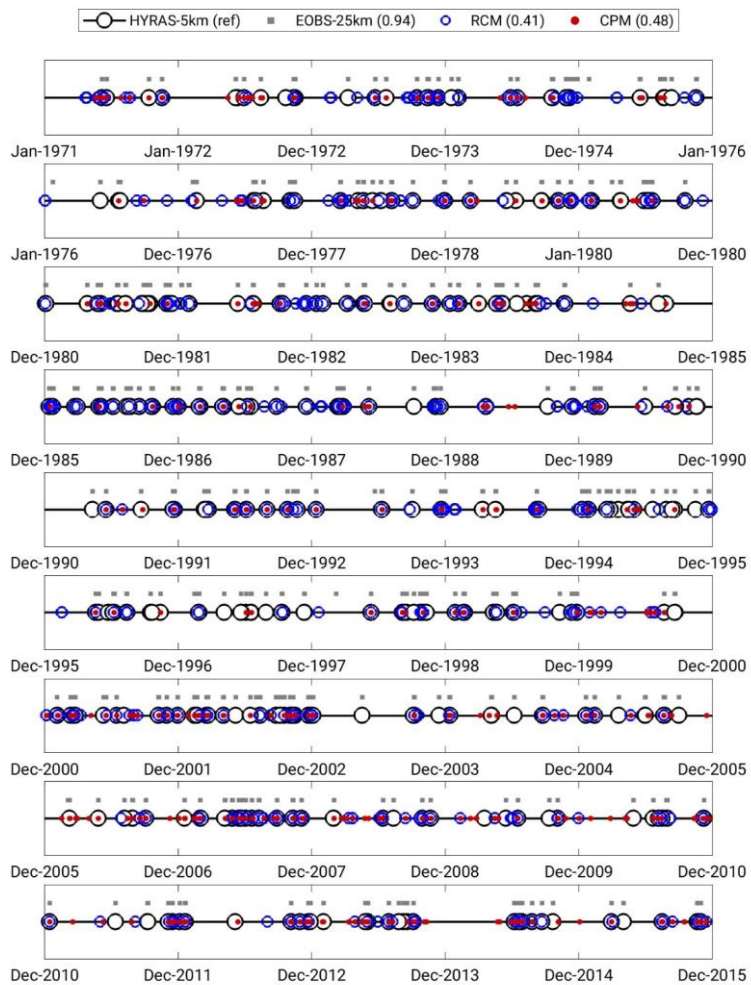
Figure 6. Dot diagram of the period 1971-2015, showing the 500 most severe precipitation events, detected using the PSI. The results are shown for HYRAS-5km (black circles), EOBS-25km (grey squares), RCM (blue circles), and CPM (red dots). The CPM data set is extended from Jan-1971 to Dec-1999 using the KLIWA-2.8km dataset (see Sect. 2.2). The spearman's rank correlation of the data sets is shown in the legend where HYRAS-5km taken as the reference. All daily precipitation datasets have been upscaled to a common grid of 25 km by means of a conservative remapping
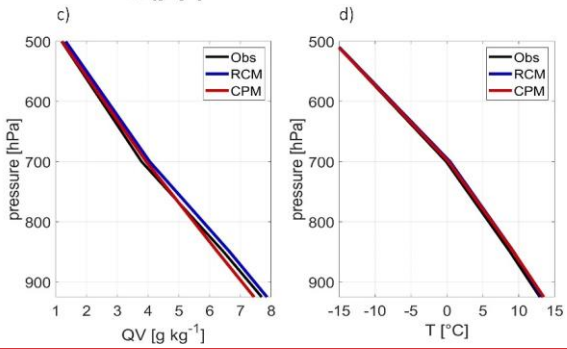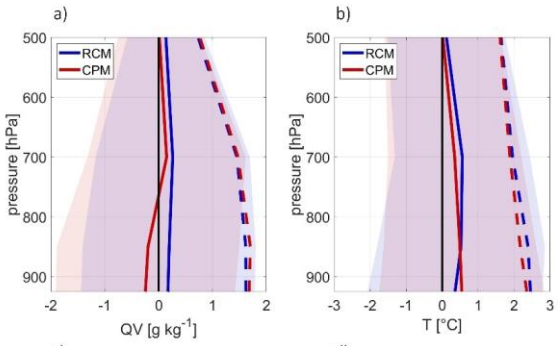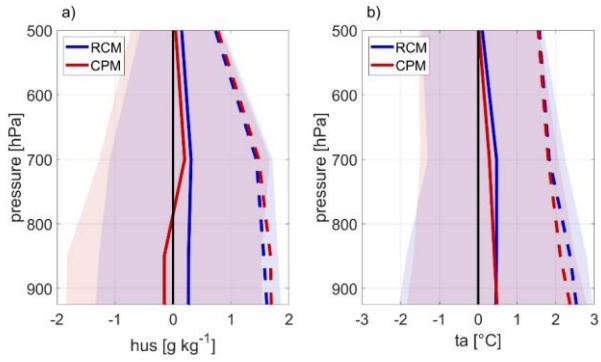
Figure 7. Validation of the model's specific humidity (a, c) and temperature (b, d) against radiosondes obtained from the UWYO soundings All available soundings during the 8 selected events (Tab. 3) are used for the validation, namely at . In total, 11 stations within the ALP-3 simulation domain (Fig. 1) are used, namely Nimes (France); Oppin, Meiningen, Idar-Oberstein, Stuttgart, Kümmersbruck and Munich (Germany); Praha (Czech Republic); Milano, S. Pietro, and Pratica di Mare (Italy). The model information is interpolated to the station location. (a, b) Show the mean bias and standard deviation of the differences (solid lines and shaded areas) as well as the RMSE (dashed lines). (c, d) show respectively the humidity and temperature profiles of RCM, CPM and the observations. The MB is calculated as MOD-OBS, hence positive MB values, indicate an overestimation of humidity or temperature.
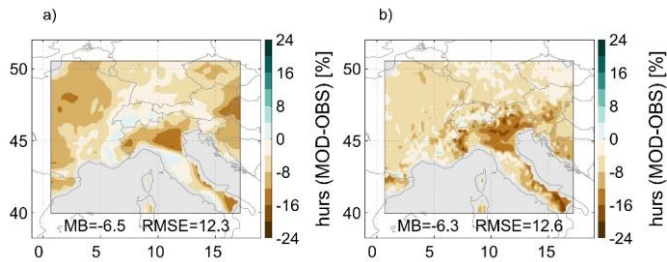
Figure 8. Spatial distributions of hursthe surface specific humidity Mean Bias (MB), obtained as differences between (a) RCM and EOBS-25km and (b) between CPM and EOBS-25km. All datasets have been coarse-grained to a 25 km resolution common grid. The spatially averaged MB and Root Mean Squared Error (RMSE) is shown in text. MB and RMSE are obtained from daily hurs surface specific humidity values for all days in the 8 selected events (Tab.3).
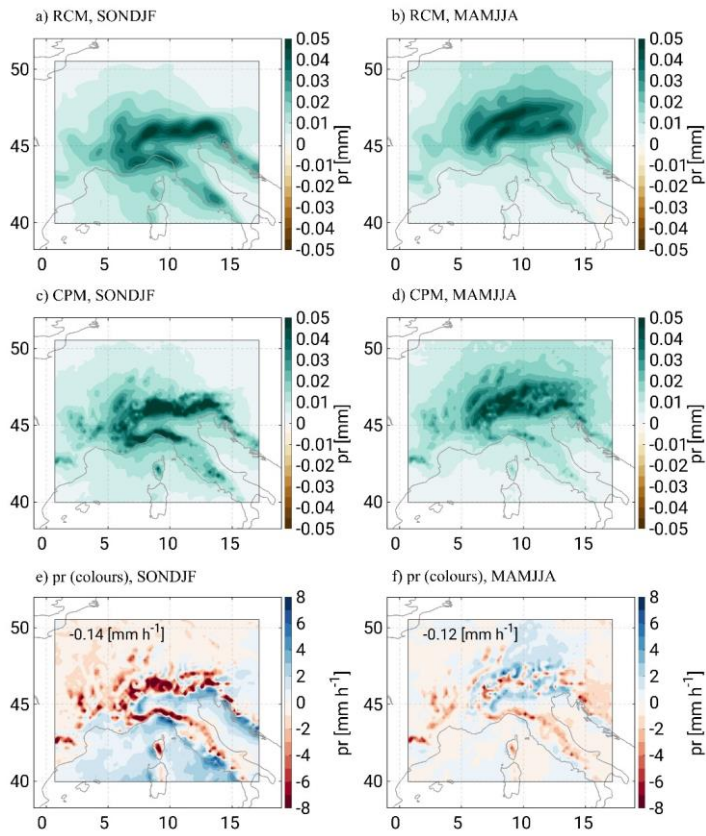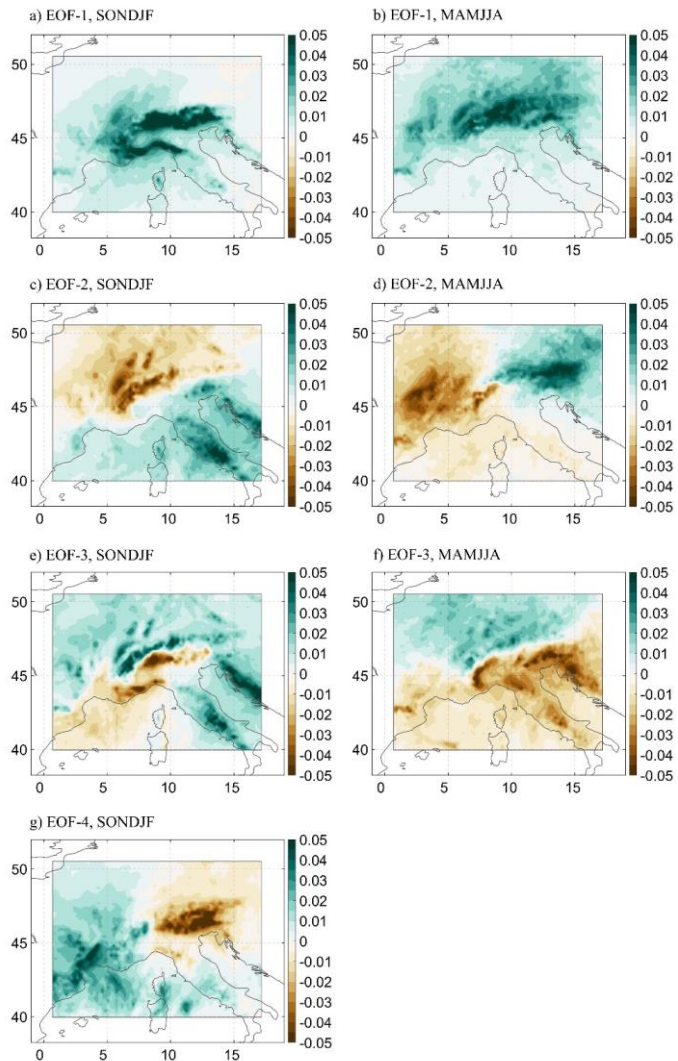
985

Figure 9. Empirical Orthogonal Function 1 of precipitation for SONDJF (a, c, e, g) and MAMJJA (b, d, f) f~~rom CPM~~or the RCM ~~(a, b) and CPM (c, d) simulations.~~ The EOF~~s-1 is~~ are obtained using the 290 most severe heavy precipitation events in each season (90-percentile). The corresponding results for RCM are shown in Fig. S.?? in the supplementary material.~~daily precipitation values~~

990 in each season (SONDJF and MAMJJA) in the period 2000-2015. The composite differences (e, f) are calculated as differences of the timely averages of precipitation on days showing PC values larger than one standard deviation, i.e, days showing a large similarity to the spatial distribution of EOF-1.
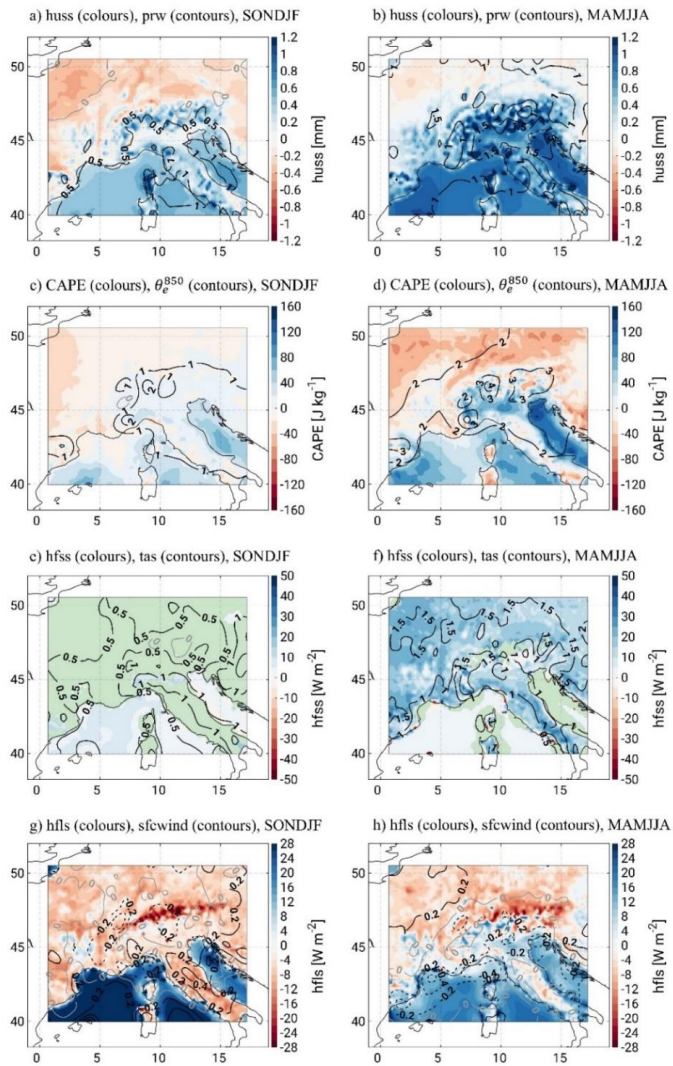
amount in CPM. The variables represented are (a, b) surface specific humidity ($huss$), precipitable water vapour (prw); (c, d); Convective Available Potential Energy ($CAPE$), equivalent potential temperature at 850 hPa (θ_e^{850}); (e, f) outbound surface sensible heat flux ($hfss$) and surface temperature (tas); (g, h) outbound surface latent heat flux ($hfls$) and surface wind speed ($sfcwind$). Green colours in $hfss$, denote grid points with no outbound sensible heat flux in RCM or CPM.
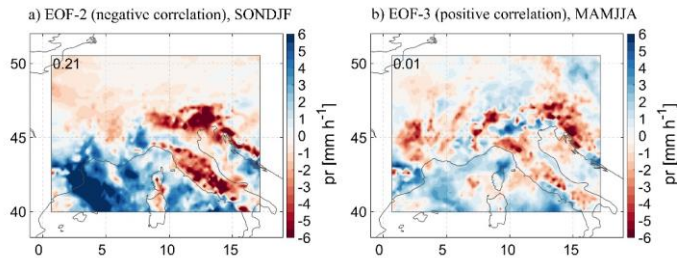
Figure 10. Composite precipitation differences between RCM (blue, positive) and CPM (red, negative). a) composites derived using the heavy precipitation days with the largest negative correlation with Winter (SONDJF) EOF-2 (Fig. 9c). b) composites derived using the heavy precipitation days with the largest negative correlation with Summer (MAMJJA) EOF-3 (Fig. 9f)
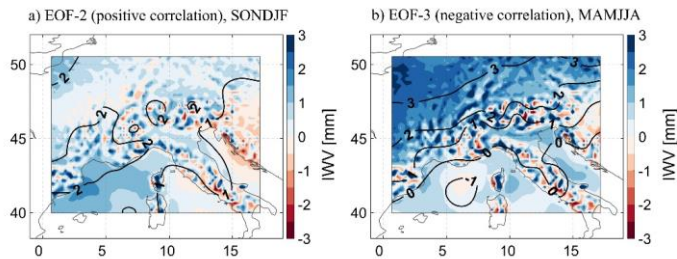
Figure 11. As Fig. 10 but for composite Integrated Water Vapour (IWV) and θ_e^{850} differences between RCM (blue, positive) and CPM (red, negative). The IWV differences are shown in a colour shading and the θ_e^{850} differences as contours. a) extended Winter (SONDJF), negative correlation of EOF-2 (Fig. 9c), b) extended Summer (MAMJJA), positive correlation of EOF-3 (Fig. 9f).

Con formato: Normal, Espacio Después: 0 pto
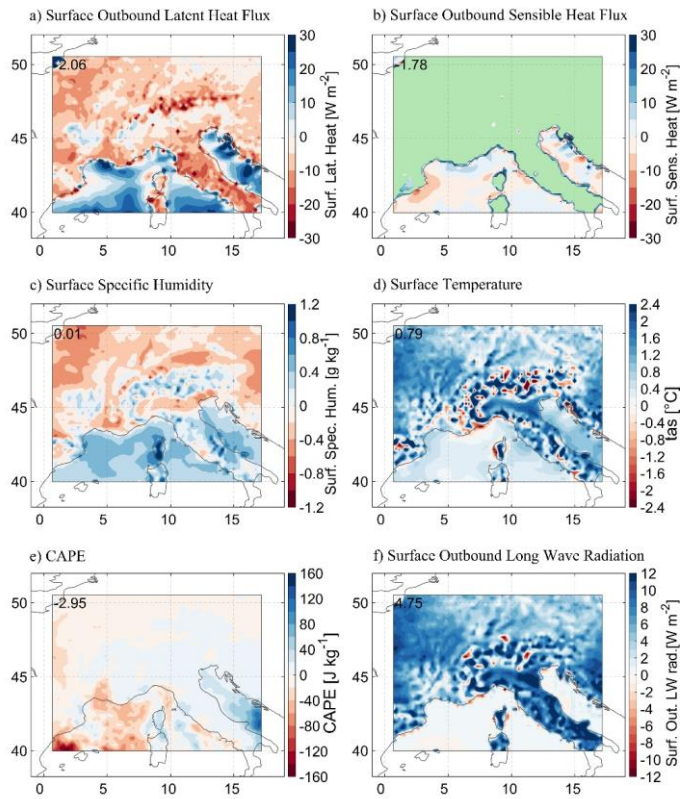
Figure 12. Composite precipitation differences between RCM (blue, positive) and CPM (red, negative). All composites correspond to the negative principal components of EOF-3 for winter (SONDFJ) events. (a) Surface outbound latent heat flux, (b) Surface outbound Sensible Heat flux, (c) Surface specific humidity, (d) Surface Temperature, (e) CAPE, (f) Surface outbound long wave radiation. Green colours in Latent and Sensible heat fluxes denote surface directed fluxes and are thus not shown.

1015

a) Surface Outbound Latent Heat Flux
b) Surface Outbound Sensible Heat Flux
c) Surface Specific Humidity
d) Surface Temperature
e) CAPE
f) Surface Outbound Long Wave Radiation
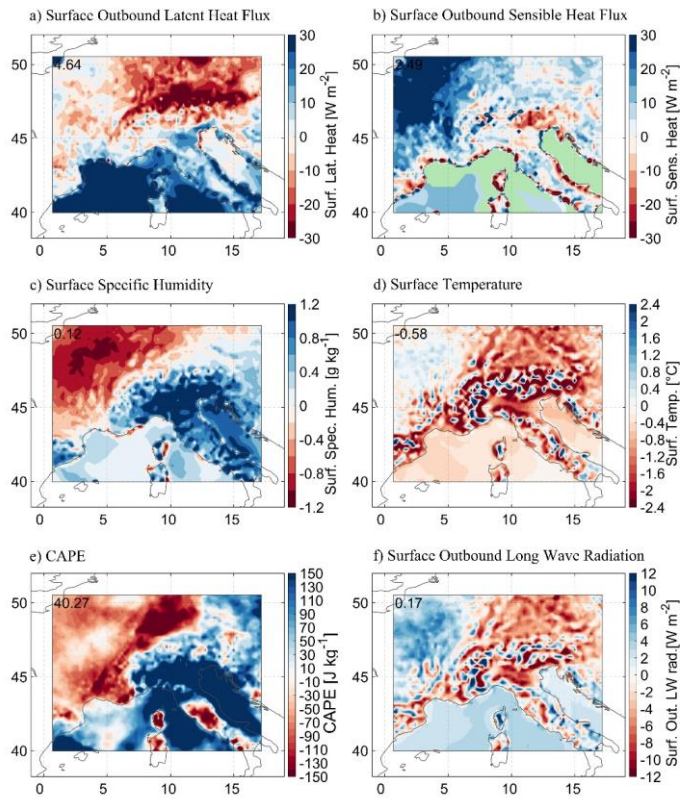
Figure 13. As Fig. 12 but for the positive principal components of EOF-2 for summer (MAMJJA) events.

Table 1. Description of observational data sets used for validation ~~of the simulations~~. The observational data ~~set~~ types used to create the different products are Radar (R), Gauges (G), Satellites (S), and Reanalysis (R).

Name	Vers.	Res.	Per.	Observations	Provider	Reference	Cover.
EOBS-25km	v20.0e	25 km, daily	1950-2020	Rain Gauges (G), surf. rel. humidity (*hurs*)	ECAD	Cornes et al., (2018)	Europe
HYRAS-5km	v2	5 km, daily	1951-2015	Rain Gauges (G)	DWD & BfG	Rauthe et al., (2013), Razafimaharo et al. (2020)	Germany

| MSWEP-11km | v2.2.0 | 11 km, 3-hly | 1979-2020 | CPC (G), GPCC (G), CMORPH (S), TMPA-3B42RT (S), GSMaP (S), ERA-Interim (R), JRA-55 (R) | GloH2O | Beck et al., (2017) | Global |
| UWYO | - | Stat.~~io ns~~, 12 hly | 2000-2015 | Radiosondes | Wyoming Univers. | http://weather.uwyo.edu/upperair/sounding.html | Global |

1025

Table 2. Reanalysis-driven COSMO-CLM decadal simulations.

Name	Res.	Param. Schemes	Lev.	Forcing	Period	Project
RCM[1]	25 km, 3-hly	Version cosmo5.0_clm9 [Fill In parametrization schemes Tiedtke convection scheme (Tiedtke, 1989)]	40	ERA-40 / ERA-int	1961-1979 / 1980-2018	Miklip-II
CPM[2]	3 km, 1-hly	[Fill In parametrization schemes] Version cosmo5.0_clm14 Only shallow convection parametrized (Tiedtke, 1989); lake parametrization (FLAKE; Mironov et al., 2010) active.	50	ERA-int	2000-2015	FPS-Convection
KLIWA-2.8km[3]	2.8 km, 1-hly	Version cosmo5.0_clm3 Only shallow convection parametrized, no lake [Fill In parametrization schemes]	49	ERA-40	1971-1999	KLIWA[3]

Con formato: Normal, Izquierda, Espacio Antes: 0 pto

Con formato: Inglés (Reino Unido)

[1] Domain covers from the Atlantic the the eastern Mediterranean from the Magreb area to Island and Scandinavia.
[2] Domain covers France, northern Italy, Switzerland, the Czech Republic, southern Germany and the Mediterranean.
1030 [3] Simulations provided by the KLIWA project (www.kliwa.de: ~~Hackenbruch et al., 2016~~Hundhausen et al., 2022). Domain covers southern Germany, Switzerland, and the eastern Czech Republic.

Table 3. Selected heavy precipitation events by means of the PSI between 2000-2015. The area considered is SGer (Fig. 1). The synoptic Weather Types (WT) have been obtained using PSML data from RCM (Sect. 3). The PSI values, total precipitation,
1035 **maximum grid point precipitation and coverage (percentage of area affected by precipitation over the 80th percentile) are obtained from HYRAS-5km.**

Event	Event days	Total. Precip. [mm]	Max. prec. [mmd^{-1}]	Coverage [%]	PSI	WT
15-Jul-2001	12-16 Jul	81098	141	83	2.22	S2
03-Nov-2002	2-5 Nov	80592	52	96	2.55	W4
13-Jan-2004	11-15 Jan	97706	103	97	3.62	W4
22-Aug-2005	19-23 Aug	106852	177	80	2.31	S4
08-Aug-2007	07-09 Aug	85473	95	89	2.79	S1
31-May-2013	31 May-02 Jun	77958	99	94	3.24	S1
08-Jul-2014	06-13 Jul	155621	83	99	3.21	S1
20-Nov-2015	19-21 Nov	102747	109	82	2.83	W1

Table 4. Relative differences of spatially and temporally aggregated precipitation ($RR_{rel.diff.}$) between the model and observations for the duration of each event (see Tab. 3), calculated as $(RR_{mod} - RR_{obs})/RR_{obs}$. **The negative signs imply an underestimation of precipitation in the model. FSS is the Fractions Skill Score between the model and the observations (Sect. 2.3.3). MSWEP-11km is used as reference. The best scores are shown for FSS values closer to 1. All datasets are upscaled to a common grid of 25 km. The investigation area is CPM (Fig.1).**

Event	$RR_{rel.diff.}$ [%]		FSS	
	RCM	CPM	RCM	CPM
15-Jul-2001	-40	-34	0.63	0.78
03-Nov-2002	-16	-11	0.81	0.82
13-Jan-2004	-7	-1	0.97	0.97
22-Aug-2005	-28	-26	0.88	0.83
08-Aug-2007	-52	-66	0.63	0.33
31-May-2013	-44	-5	0.26	0.87
08-Jul-2014	-6	-21	0.96	0.9
20-Nov-2015	-18	-17	0.92	0.93
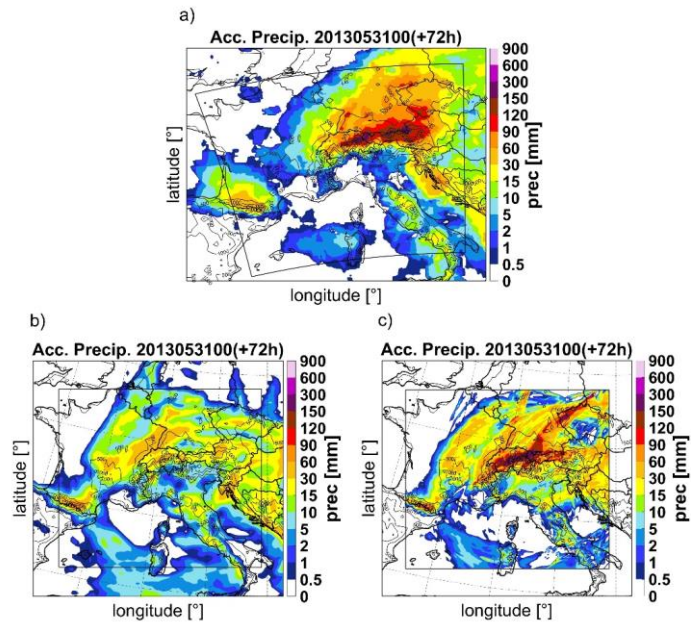
Figure S1. Spatial distribution of 72h accumulated precipitation for the event 31-May-2013 as observed by MSWEP-11km (a) and simulated by RCM (b) and CPM (c). The contours represent the surface height.
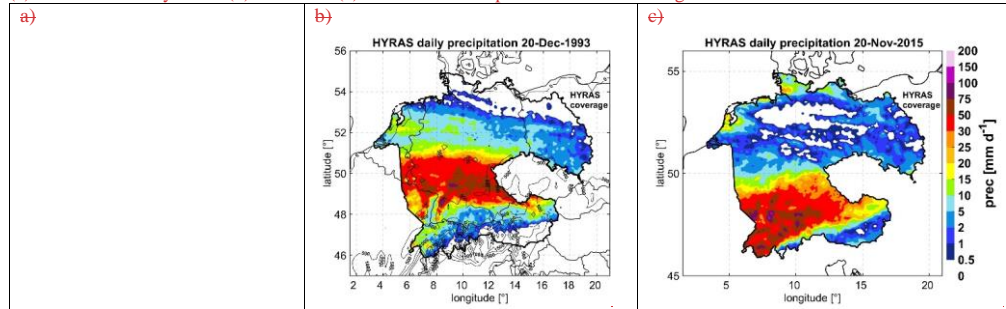
Figure S2. (a) Spatial distribution of the percentile-80 of precipitation climatology in the period 1975-2015 for HYRAS-5km. (b) Spatial distribution of daily precipitation during the 20-Dec-1993 and (c) the 20-Nov-2015.
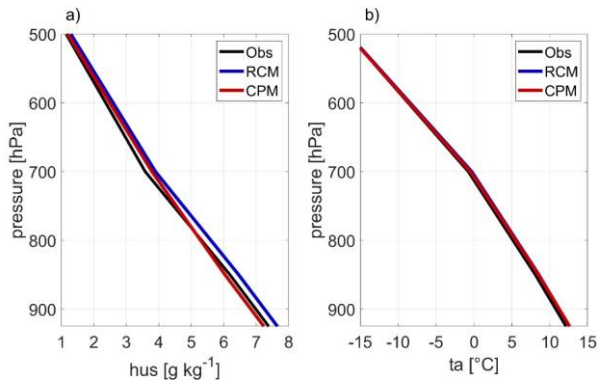
Figure S2. Vertical profiles of specific humidity (a) and temperature (b), timely averaged for all time steps of the 8 selected events in Tab. 3 for 11 stations. The UWYO soundings are shown in black, RCM in blue and CPM in red. The corresponding MB and RMSE are shown in Fig. 7.

1055
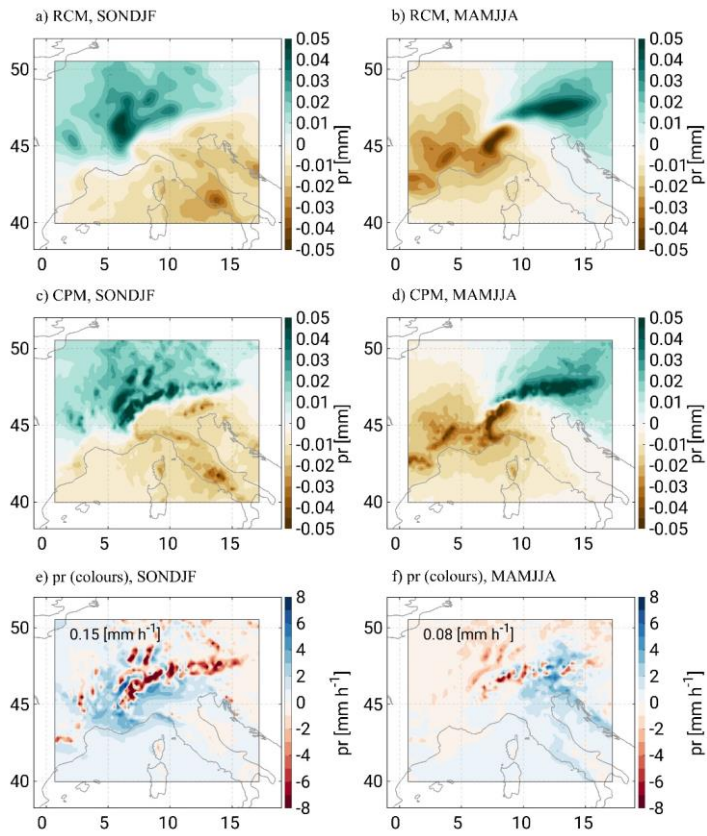
Figure S3. As Fig. 9 but for EOF 2.
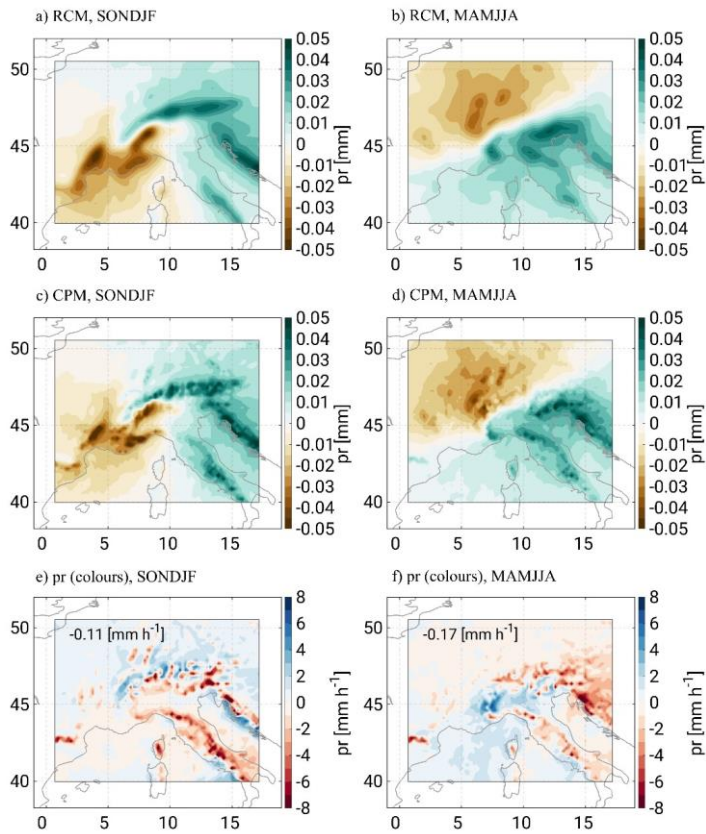
Figure S4. As Fig.9 but for EOF-3.
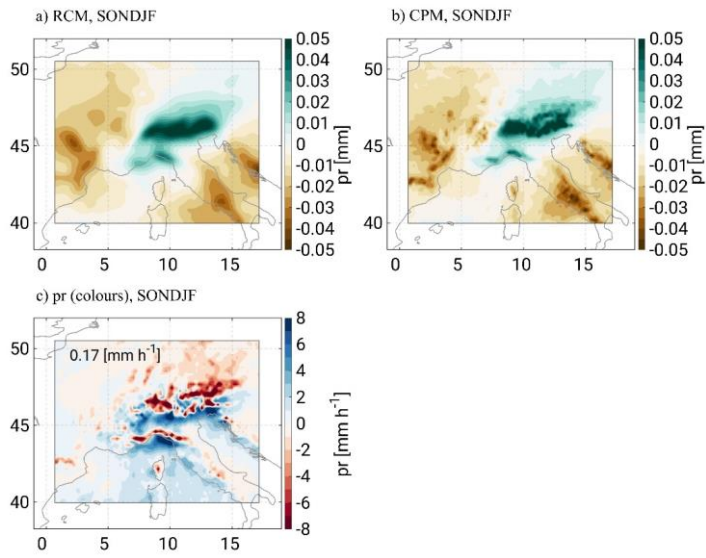
Figure S5. As Fig.9 but for EOF-4

1065
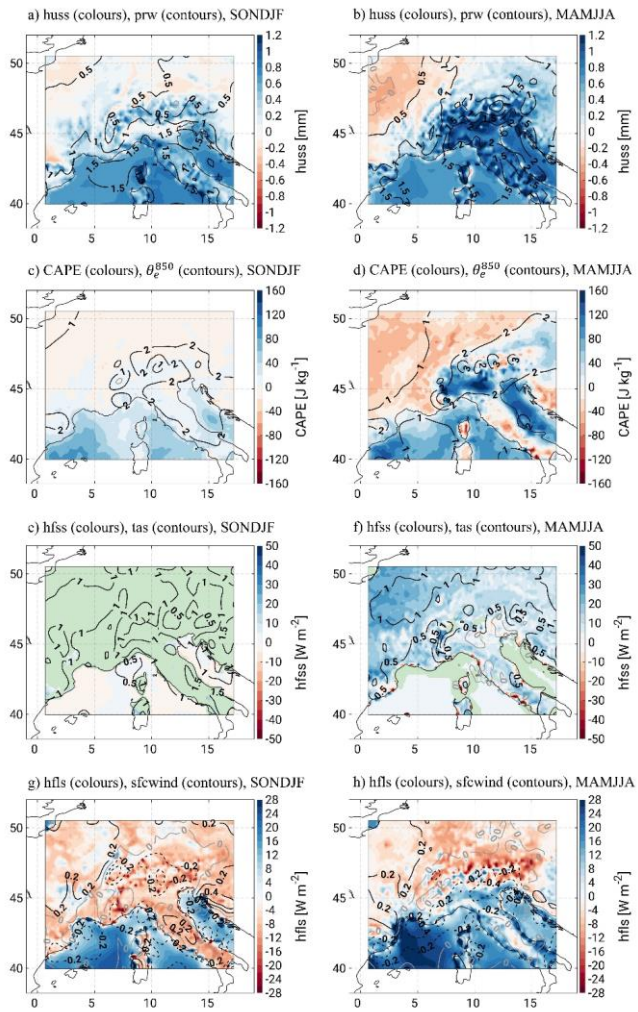
Figure S6. As Fig. 10 but for EOF-2
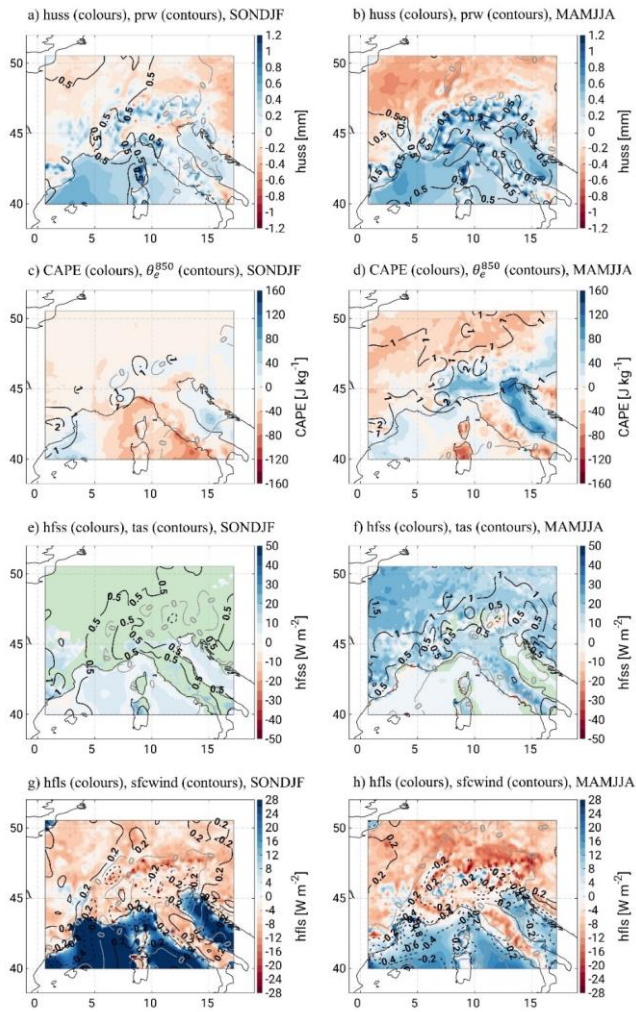
Figure S7. As Fig. 10 but for EOF-3

1070
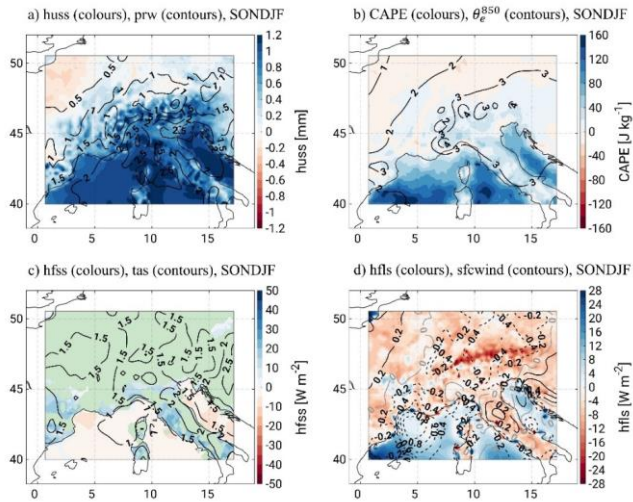
Figure S8. As Fig. 10 but for EOF-4

11 Code availability

The COSMO-CLM is available for member of the CLM community and the documentation is accessible at, http://www.cosmo-model.org/content/model/documentation/core/default.htm (last accessed, 11-Aug-2021).

11 Data availability

The EOBS-25km dataset is accessible after registration at https://www.ecad.eu/download/ensembles/download.php#version (last accessed, 17-Dec-2021). The HYRAS-5km data set is publicly accessible at the Climate Data Centre (CDC) of the German Weather Service (DWD) at https://opendata.dwd.de/climate_environment/CDC (last accessed, 17-Dec-2021) MSWEP-11km, has been provided by the Climate Prediction Centre, after agreement of use. The soundings from UWYO are publicly accessible at http://weather.uwyo.edu/upperair/sounding.html (last accessed, 17-Dec-2021). Further information about the XCES tool can be found in (https://www.xces.dkrz.de/)

13 Author contribution

ACA, HF, and JGP designed the study. ELE implemented the PSI index in the Mistral at the DKRZ. ACA and HF analysed the data. ACA prepared the figures and wrote the initial draft. All authors contributed with discussions and revisions.

14 Competing interests

The authors declare that they have no conflict of interest.

14 Acknowledgements

The research was accomplished within project A1 "SEVERE - Scale Dependent Process Representation and Sensitivity Analysis for Most Extreme Events" (Grant No. 01 LP 1901 A) and D2 "COSOX – Coordination of Software Management" (Grant No. 01 LP 1904 B) within the German Federal Ministry of Education and Research (BMBF) research initiative ClimXtreme. JGP thanks the AXA research fund for support. We would like to thank Deborah Niermann and Stella Steidl at the (German Weather Service, DWD) for providing the HYRAS data set. We would like to thank Hylke Beck for sharing the MSWEP precipitation data. Moreover, we would like to acknowledge M. Lemus-Canovas for providing the SynoptReg R package used for computing the synoptic weather types (Lemus-Canovas et al., 2019). We acknowledge the contribution of the DKRZ for storing and maintaining the model data and the FUB for the software coordination of XCES.

15 References

Alfieri, L., Feyen, L., Salamon, P., Thielen, J., Bianchi, A., Dottori, F., and Burek, P.: Modelling the socio-economic impact of river floods in Europe, Natural Hazards and Earth System Sciences, 16, 1401–1411, https://doi.org/10.5194/nhess-16-1401-2016, 2016.

Ban, N., Schmidli, J., and Schär, C.: Evaluation of the convection-resolving regional climate modeling approach in decade-long simulations, Journal of Geophysical Research: Atmospheres, 119, 7889–7907, https://doi.org/10.1002/2014jd021478, 2014.

Ban, N., Rajczak, J., Schmidli, J., and Schär, C.: Analysis of Alpine precipitation extremes using generalized extreme value theory in convection-resolving climate simulations, Climate Dynamics, 55, 61–75, https://doi.org/10.1007/s00382-018-4339-4, 2018.

Ban, N., Caillaud, C., Coppola, E., Pichelli, E., Sobolowski, S., Adinolfi, M., Ahrens, B., Alias, A., Anders, I., Bastin, S., Belušiˊc, D., Berthou, S., Brisson, E., Cardoso, R. M., Chan, S. C., Christensen, O. B., Fernández, J., Fita, L., Frisius, T., Gašparac, G., Giorgi, F., Goergen, K., Haugen, J. E., Hodnebrog, Ø., Kartsios, S., Katragkou, E., Kendon, E. J., Keuler, K., Lavin-Gullon, A., Lenderink, G., Leutwyler, D., Lorenz, T., Maraun, D., Mercogliano, P., Milovac, J., Panitz, H.-J., Raffa, M., Remedio, A. R., Schär, C., Soares, P. M. M., Srnec, L., Steensen, B. M., Stocchi, P., Tölle, M. H., Truhetz, H., Vergara-Temprado, J., de Vries, H., Warrach-Sagi, K., Wulfmeyer, V., and Zander, M. J.: The first multi-model ensemble of regional climate simulations at kilometer-scale resolution, part I: evaluation of precipitation, Climate Dynamics, 57, 275–302, https://doi.org/10.1007/s00382-021-05708-w, 2021.

Baldauf, M., Seifert, A., Förstner, J., Majewski, D., Raschendorfer, M., and Reinhardt, T.: Operational convective-scale numerical weather prediction with the COSMO model: Description and sensitivities, Mon. Weather Rev., 139, 3887–3905, https://doi.org/10.1175/MWR-D-10-05013.1, 2011 .

Bandhauer, M., Isotta, F., Lakatos, M., Lussana, C., Båserud, L., Izsák, B., Szentes, O., Tveito, O. E., and Frei, C.: Evaluation of daily precipitation analyses in E-OBS (v19.0e) and ERA5 by comparison to regional high-resolution datasets in European regions, International Journal of Climatology, https://doi.org/10.1002/joc.7269, 2021.

Barthlott, C. and Hoose, C.: Spatial and temporal variability of clouds and precipitation over Germany: multiscale simulations across the "gray zone", Atmospheric Chemistry and Physics, 15, 12 361–12 384, https://doi.org/10.5194/acp-15-12361-2015, 2015.

Bastin, S., Drobinski, P., Chiriaco, M., Bock, O., Roehrig, R., Gallardo, C., Conte, D., Alonso, M. D., Li, L., Lionello, P., and Parracho, A. C.: Impact of humidity biases on light precipitation occurrence: observations versus simulations, Atmospheric Chemistry and Physics, 19, 1471–1490, https://doi.org/10.5194/acp-19-1471-2019, 2019.

Beck, H. E., van Dijk, A. I. J. M., Levizzani, V., Schellekens, J., Miralles, D. G., Martens, B., and de Roo, A.: MSWEP: 3-hourly 0.25° global gridded precipitation (1979–2015) by merging gauge, satellite, and reanalysis data, Hydrology and Earth System Sciences, 21, 589–615, https://doi.org/10.5194/hess-21-589-2017, 2017.

Beck, H. E., Pan, M., Roy, T., Weedon, G. P., Pappenberger, F., van Dijk, A. I. J. M., Huffman, G. J., Adler, R. F., and Wood, E. F.: Daily evaluation of 26 precipitation datasets using Stage-IV gauge-radar data for the CONUS, Hydrology and Earth System Sciences, 23, 207–224, 2019.

Berg, P., Christensen, O. B., Klehmet, K., Lenderink, G., Olsson, J., Teichmann, C., and Yang, W.: Summertime precipitation extremes in a EURO-CORDEX 0.11° ensemble at an hourly resolution, Natural Hazards and Earth System Sciences, 19, 957–971, https://doi.org/10.5194/nhess-19-957-2019, 2019.

Berthou, S., Kendon, E. J., Chan, S. C., Ban, N., Leutwyler, D., Schär, C., and Fosser, G.: Pan-European climate at convection-permitting scale: a model intercomparison study, Climate Dynamics, 55, 35–59, https://doi.org/10.1007/s00382-018-4114-6, 2018.

Berthou, S., Rowell, D. P., Kendon, E. J., Roberts, M. J., Stratton, R. A., Crook, J. A., and Wilcox, C.: Improved climatological precipitation characteristics over West Africa at convection-permitting scales, Climate Dynamics, 53, 1991–2011, https://doi.org/10.1007/s00382-019-04759-4, 2019.

Bui, H. X., Yu, J.-Y., and Chou, C.: Impacts of model spatial resolution on the vertical structure of convection in the tropics, Climate Dynamics, 52, 15–27, https://doi.org/10.1007/s00382-018-4125-3, 2018.

Caldas-Alvarez, A. and Khodayar, S.: Assessing atmospheric moisture effects on heavy precipitation during HyMeX IOP16 using GPS nudging and dynamical downscaling, Natural Hazards and Earth System Sciences, 20, 2753–2776, https://doi.org/10.5194/nhess-202753-2020, 2020.

Caldas-Alvarez, A., Khodayar, S., and Knippertz, P.: The impact of GPS and high-resolution radiosonde nudging on the simulation of heavy precipitation during HyMeX IOP6, Weather and Climate Dynamics, 2, 561–580, https://doi.org/10.5194/wcd-2-561-2021, 2021.

Chan, S. C., Kendon, E. J., Fowler, H. J., Blenkinsop, S., Ferro, C. A. T., and Stephenson, D. B.: Does increasing the spatial resolution of a regional climate model improve the simulated daily precipitation?, Climate Dynamics, 41, 1475–1495, https://doi.org/10.1007/s00382-012-1568-9, 2012.

Ciesielski, P. E., Yu, H., Johnson, R. H., Yoneyama, K., Katsumata, M., Long, C. N., Wang, J., Loehrer, S. M., Young, K., Williams, S. F., Brown, W., Braun, J., and Hove, T. V.: Quality-Controlled Upper-Air Sounding Dataset for DYNAMO/CINDY/AMIE: Development and Corrections, Journal of Atmospheric and Oceanic Technology, 31, 741–764, https://doi.org/10.1175/jtech-d-13-00165.1, 2014.

Coppola, E., Sobolowski, S., Pichelli, E., Raffaele, F., Ahrens, B., Anders, I., Ban, N., Bastin, S., Belda, M., Belusic, D., Caldas-Alvarez, A., Cardoso, R. M., Davolio, S., Dobler, A., Fernandez, J., Fita, L., Fumiere, Q., Giorgi, F., Goergen, K., Güttler, I., Halenka, T., Heinzeller, D., Hodnebrog, Ø., Jacob, D., Kartsios, S., Katragkou, E., Kendon, E., Khodayar, S., Kunstmann, H., Knist, S., Lavín-Gullón, A., Lind, P., Lorenz, T., Maraun, D., Marelle, L., van Meijgaard, E., Milovac, J., Myhre, G., Panitz, H.-J., Piazza, M., Raffa, M., Raub, T., Rockel, B., Schär, C., Sieck, K., Soares, P. M. M., Somot, S., Srnec, L., Stocchi, P., Tölle, M. H., Truhetz, H., Vautard, R., de Vries, H., and Warrach-Sagi, K.: A first-of-its-kind multi-model convection permitting ensemble for investigating convective phenomena over Europe and the Mediterranean, Climate Dynamics, 55, 3–34, https://doi.org/10.1007/s00382-018-4521-8, 2018.

Cornes, R. C., van der Schrier, G., van den Besselaar, E. J. M., and Jones, P. D.: An Ensemble Version of the E-OBS Temperature and Precipitation Data Sets, Journal of Geophysical Research: Atmospheres, 123, 9391–9409, https://doi.org/10.1029/2017jd028200, 2018.

Doswell, C. A., Brooks, H. E., and Maddox, R. A.: Flash Flood Forecasting: An Ingredients-Based Methodology, Weather and Forecasting, 11, 560–581, https://doi.org/10.1175/1520-0434(1996)011<0560:fffaib>2.0.co;2, 1996.

Du, Y., Wang, D., Zhu, J., Lin, Z., and Zhong, Y.: Intercomparison of multiple high-resolution precipitation products over China: Climatology and extremes, Atmospheric Research, 278, 106342, 2022.

Emanuel, K. A.: Atmospheric Convection, OXFORD UNIV PR, https://www.ebook.de/de/product/3606238/kerry_a_emanuel_atmospheric convection.html, 1994.

Feldmann, H., g. Pinto, J., Laube, N., Uhlig, M., Moemken, J., Pasternack, A., Früh, B., Pohlmann, H., and Kottmeier, C.: Skill and added value of the MiKlip regional decadal prediction system for temperature over Europe, Tellus A: Dynamic Meteorology and Oceanography, 71, 1618 678, https://doi.org/10.1080/16000870.2019.1618678, 2019.

Fosser, G., Khodayar, S., and Berg, P.: Benefit of convection permitting climate model simulations in the representation of convective precipitation, Climate Dynamics, 44, 45–60, https://doi.org/10.1007/s00382-014-2242-1, 2014.

Fuchs, T., Rapp, J., and Rudolf, B.: Starkniederschläge im Oktober 1998 in Mittel- undWesteuropa, Special report, German Weather Service (DWD), 1998.

Hackenbruch, J., Schädler, G., and Schipper, J. W.: Added value of high-resolution regional climate simulations for regional impact studies, Meteorologische Zeitschrift, 25, 291–304, https://doi.org/10.1127/metz/2016/0701, 2016.

Heim, C.: The Influence of the Resolution of Topography and Surface Fields on the Simulation of Orographic Moist Convection, https://doi.org/10.3929/ETHZ-B-000288269, 2018.

Heim, C., Panosetti, D., Schlemmer, L., Leuenberger, D., and Schär, C.: The Influence of the Resolution of Orography on the Simulation of Orographic Moist Convection, Monthly Weather Review, 148, 2391–2410, https://doi.org/10.1175/mwr-d-19-0247.1, 2020.

Hohenegger, C., Brockhaus, P., Bretherton, C. S., and Schär, C.: The Soil Moisture–Precipitation Feedback in Simulations with Explicit and Parameterized Convection, Journal of Climate, 22, 5003–5020, https://doi.org/10.1175/2009jcli2604.1, 2009.

Holton, J.: An introduction to dynamic meteorology, Academic Press, Amsterdam Boston, 2013.

Hu, G. and Franzke, C. L. E.: Evaluation of Daily Precipitation Extremes in Reanalysis and Gridded Observation-Based Data Sets Over Germany, Geophysical Research Letters, 47, https://doi.org/10.1029/2020gl089624, 2020.

Hundhausen, M., Feldmann, H., Laube, N., and Pinto, J. G.: Future heat extremes and impacts in a convection permitting climate ensemble over Germany, Nat. Hazards Earth Syst. Sci. Discuss. [preprint], https://doi.org/10.5194/nhess-2022-283, in review, 2022.

Jacob, D., Petersen, J., Eggert, B., Alias, A., Christensen, O. B., Bouwer, L. M., Braun, A., Colette, A., Déqué, M., Georgievski, G., Georgopoulou, E., Gobiet, A., Menut, L., Nikulin, G., Haensler, A., Hempelmann, N., Jones, C., Keuler, K., Kovats, S., Kröner, N., Kotlarski, S., Kriegsmann, A., Martin, E., van Meijgaard, E., Moseley, C., Pfeifer, S., Preuschmann, S., Radermacher, C., Radtke, K., Rechid, D., Rounsevell, M., Samuelsson, P., Somot, S., Soussana, J.-F., Teichmann, C., Valentini, R., Vautard, R., Weber, B., and Yiou, P.: EURO-CORDEX: new high-resolution climate change projections for European impact research, Regional Environmental Change, 14, 563–578, https://doi.org/10.1007/s10113-013-0499-2, 2013.

Jolliffe, I. T.: Principal Component Analysis, Springer-Verlag GmbH, New York, https://www.ebook.de/de/product/2047838/i_t_jolliffe_principal_component_analysis.html, 2002.

Kautz, L.-A., Martius, O., Pfahl, S., Pinto, J. G., Ramos, A. M., Sousa, P. M., and Woollings, T.: Atmospheric Blocking and Weather Extremes over the Euro-Atlantic Sector – A Review, Weather Clim. Dynam. Discuss. [preprint], https://doi.org/10.5194/wcd-2021-56, in review, 2021.

Keil, C., Chabert, L., Nuissier, O., and Raynaud, L.: Dependence of predictability of precipitation in the northwestern Mediterranean coastal region on the strength of synoptic control, Atmospheric Chemistry and Physics, 20, 15 851–15 865, https://doi.org/10.5194/acp-20-15851- 2020, 2020.

Kelemen, F. D., Ludwig, P., Reyers, M., Ulbrich, S., and Pinto, J. G.: Evaluation of moisture sources for the Central European
summer flood of May/June 2013 based on regional climate model simulations, Tellus A: Dynamic Meteorology and
Oceanography, 68, 29 288, https://doi.org/10.3402/tellusa.v68.29288, 2016.

Kendon, E. J., Roberts, N. M., Senior, C. A., and Roberts, M. J.: Realism of Rainfall in a Very High-Resolution Regional
Climate Model, Journal of Climate, 25, 5791–5806, https://doi.org/10.1175/jcli-d-11-00562.1, 2012.

Khodayar, S., Davolio, S., Girolamo, P. D., Brossier, C. L., Flaounas, E., Fourrie, N., Lee, K.-O., Ricard, D., Vie, B., Bouttier,
F., Caldas-Alvarez, A., and Ducrocq, V.: Overview towards improved understanding of the mechanisms leading to
heavy precipitation in the western Mediterranean: lessons learned from HyMeX, Atmospheric Chemistry and Physics,
21, 17 051–17 078, https://doi.org/10.5194/acp-21-17051-2021, 2021.

Knippertz, P., Christoph, M. & Speth, P. Long-term precipitation variability in Morocco and the link to the large-scale
circulation in recent and future climates. Meteorol Atmos Phys 83, 67–88 (2003). https://doi.org/10.1007/s00703-
002-0561-y

Langhans, W., Schmidli, J., and Schär, C.: Mesoscale Impacts of Explicit Numerical Diffusion in a Convection-Permitting
Model, Monthly Weather Review, 140, 226–244, https://doi.org/10.1175/2011mwr3650.1, 2012.

Leckebusch, G. C., Renggli, D., and Ulbrich, U.: Development and application of an objective storm severity measure for the
Northeast Atlantic region, Meteorologische Zeitschrift, 17, 575–587, https://doi.org/10.1127/0941-2948/2008/0323,
2008.

Lemus-Canovas, M., Lopez-Bustins, J. A., Trapero, L., and Martin-Vide, J.: Combining circulation weather types and daily
precipitation modelling to derive climatic precipitation regions in the Pyrenees, Atmospheric Research, 220, 181–
193, https://doi.org/10.1016/j.atmosres.2019.01.018, 2019.

Li, P., Furtado, K., Zhou, T., Chen, H., and Li, J.: Convection-permitting modelling improves simulated precipitation over the
central and eastern Tibetan Plateau, Quarterly Journal of the Royal Meteorological Society, 147, 341–362,
https://doi.org/10.1002/qj.3921, 2020.

Lin, C., Chen, D., Yang, K., and Ou, T.: Impact of model resolution on simulating the water vapor transport through the central
Himalayas: implication for models' wet bias over the Tibetan Plateau, Climate Dynamics, 51, 3195–3207,
https://doi.org/10.1007/s00382-018-4074-x, 2018.

Lucas-Picher, P., Argüeso, D., Brisson, E., Tramblay, Y., Berg, P., Lemonsu, A., Kotlarski, S., and Caillaud, C.: Convection
-permitting modeling with regional climate models: Latest developments and next steps, WIREs Climate Change, 12,
https://doi.org/10.1002/wcc.731, 2021.

Massacand, A. C., Wernli, H., and Davies, H. C.: Heavy precipitation on the alpine southside: An upper-level precursor, Geophysical Research Letters, 25, 1435–1438, https://doi.org/10.1029/98gl50869, 1998.

1245 Meredith, E. P., Maraun, D., Semenov, V. A., and Park, W.: Evidence for added value of convection-permitting models for studying changes in extreme precipitation, Journal of Geophysical Research: Atmospheres, 120, 12 500–12 513, https://doi.org/10.1002/2015jd024238, 2015a.

Meredith, E. P., Semenov, V. A., Maraun, D., Park, W., and Chernokulsky, A. V.: Crucial role of Black Sea warming in amplifying the 2012 Krymsk precipitation extreme, Nature Geoscience, 8, 615–619, 1250 https://doi.org/10.1038/ngeo2483, 2015b

Meredith, E. P., Ulbrich, U., and Rust, H. W.: Subhourly rainfall in a convection-permitting model, Environmental Research Letters, 15, 034 031, https://doi.org/10.1088/1748-9326/ab6787, 2020.

Mironov, D., E. Heise, E. Kourzeneva, B. Ritter, N. Schneider, and A. Terzhevik, 2010: Implementation of the lake parameterisation scheme FLake into the numerical weather prediction model COSMO. Boreal Env. Res., 15, 218–1255 230, http://www.borenv.net/BER/archive/pdfs/ber15/ber15-218.pdf

North, G. R., Moeng, F. J., Bell, T. L., and Cahalan, R. F.: The Latitude Dependence of the Variance of Zonally Averaged Quantities, Monthly Weather Review, 110, 319–326, https://doi.org/10.1175/1520-0493(1982)110<0319:tldotv>2.0.co;2, 1982.

Panosetti, D., Schlemmer, L., and Schär, C.: Convergence behavior of idealized convection-resolving simulations of 1260 summertime deep moist convection over land, Climate Dynamics, 55, 215–234, https://doi.org/10.1007/s00382-018-4229-9, 2018.

Peña-Guerrero, M. D., Umirbekov, A., Tarasova, L., and Müller, D.: Comparing the performance of high-resolution global precipitation products across topographic and climatic gradients of Central Asia, International Journal of Climatology, 42, 5554–5569, 2022.

1265 Peres-Neto, P. R., Jackson, D. A., and Somers, K. M.: How many principal components? stopping rules for determining the number of non-trivial axes revisited, Computational Statistics & Data Analysis, 49, 974–997, https://doi.org/10.1016/j.csda.2004.06.015, 2005.

Pichelli, E., Coppola, E., Sobolowski, S., Ban, N., Giorgi, F., Stocchi, P., Alias, A., Beluši ́c, D., Berthou, S., Caillaud, C., Cardoso, R. M., Chan, S., Christensen, O. B., Dobler, A., de Vries, H., Goergen, K., Kendon, E. J., Keuler, K., 1270 Lenderink, G., Lorenz, T., Mishra, A. N., Panitz, H.-J., Schär, C., Soares, P. M. M., Truhetz, H., and Vergara-Temprado, J.: The first multi-model ensemble of regional climate simulations at kilometer-scale resolution part 2: historical and future simulations of precipitation, Climate Dynamics, https://doi.org/10.1007/s00382-021-05657-4, 2021.

Pinto, J., Karremann, M., Born, K., Della-Marta, P., and Klawa, M.: Loss potentials associated with European windstorms under future climate conditions, Climate Research, 54, 1–20, https://doi.org/10.3354/cr01111, 2012.

Piper, D., Kunz, M., Ehmele, F., Mohr, S., Mühr, B., Kron, A., and Daniell, J.: Exceptional sequence of severe thunderstorms and related flash floods in May and June 2016 in Germany – Part 1: Meteorological background, Natural Hazards and Earth System Sciences, 16, 2835–2850, https://doi.org/10.5194/nhess-16-2835-2016, 2016.

Prein, A. F., Langhans, W., Fosser, G., Ferrone, A., Ban, N., Goergen, K., Keller, M., Tölle, M., Gutjahr, O., Feser, F., Brisson, E., Kollet, S., Schmidli, J., Lipzig, N. P. M., and Leung, R.: A review on regional convection-permitting climate modeling: Demonstrations, prospects, and challenges, Reviews of Geophysics, 53, 323–361, https://doi.org/10.1002/2014rg000475, 2015.

Prein, A. F., Rasmussen, R., Castro, C. L., Dai, A., and Minder, J.: Special issue: Advances in convection-permitting climate modeling,Climate Dynamics, 55, 1–2, https://doi.org/10.1007/s00382-020-05240-3, 2020.

Preisendorfer, R.: Principal component analysis in meteorology and oceanography, Elsevier Distributors for the U.S. and Canada, Elsevier Science Pub. Co, Amsterdam New York New York, NY, U.S.A, 1988.

Prellberg, D. and Fell, E.: Rheinhochwasser März 1988 Hochwasserablauf und meldedienst, Tech. Rep. 226, Landesamt für Wasserwirtschafft Rheinland Pfalz, 1989.

Purr, C., Brisson, E., and Ahrens, B.: Convective Shower Characteristics Simulated with the Convection-Permitting Climate Model COSMO-CLM, Atmosphere, 10, 810, https://doi.org/10.3390/atmos10120810, 2019.

Rajczak, J., Pall, P., and Schär, C.: Projections of extreme precipitation events in regional climate simulations for Europe and the Alpine Region, Journal of Geophysical Research: Atmospheres, 118, 3610–3626, https://doi.org/10.1002/jgrd.50297, 2013.

Ranasinghe, R., Ruane, A., Vautard, R., Arnell, N., Coppola, E., Cruz, F., Dessai, S., Islam, A., Rahimi, M., RuizCarrascal, D., Sillmann, J., Sylla, M., Tebaldi, C., Wang, W., and Zaaboul, R.: Climate Change Information for Regional Impact and for Risk Assessment. In Climate Change 2021: The Physical Science Basis. Contribution ofWorking Group I to the Sixth Assessment Report of the Intergovernmental Panel on Climate Change [MassonDelmotte, V., P. Zhai, A. Pirani, S.L. Connors, C. Péan, S. Berger, N. Caud, Y. Chen, L. Goldfarb, M.I. Gomis, M.Huang, K. Leitzell, E. Lonnoy, J.B.R. Matthews, T.K. Maycock, T. Waterfield, O. Yelekçi, R. Yu, and B. Zhou (eds.)], Tech. rep., Cambridge University Press, 2021.

Rauthe, M., Steiner, H., Riediger, U., Mazurkiewicz, A., and Gratzki, A.: A Central European precipitation climatology Part I: Generation and validation of a high-resolution gridded daily data set (HYRAS), Meteorologische Zeitschrift, 22, 235–256, https://doi.org/10.1127/0941-2948/2013/0436, 2013.

Razafimaharo, C., Krähenmann, S., Höpp, S., Rauthe, M., and Deutschländer, T.: New high-resolution gridded dataset of daily mean, minimum, and maximum temperature and relative humidity for Central Europe (HYRAS), Theoretical and Applied Climatology, 142, 1531–1553, https://doi.org/10.1007/s00704-020-03388-w, 2020.

Risanto, C. B., Castro, C. L., Moker, J. M., Arellano, A. F., Adams, D. K., Fierro, L. M., and Sosa, C. M. M.: Evaluating Forecast Skills of Moisture from Convective-Permitting WRF-ARW Model during 2017 North American Monsoon Season, Atmosphere, 10, 694, https://doi.org/10.3390/atmos10110694, 2019.

Roberts, N. M. and Lean, H. W.: Scale-Selective Verification of Rainfall Accumulations from High-Resolution Forecasts of Convective Events, Monthly Weather Review, 136, 78–97, https://doi.org/10.1175/2007mwr2123.1, 2008.

Rockel, B., Will, A., and Hense, A.: The regional climate model COSMO-CLM (CCLM), Meteorol. Z., 17, 347–348, https://doi.org/10.1127/0941-2948/2008/0309, 2008. a, b, c

Schacher, F. and Gerstgrasser, D.: Aussergewöhnliche Gewitterlage im Juni 2007, Technical report, MeteoSchweiz, 2007.

Schäfer, A., Mühr, B., Daniell, J., Ehret, U., Ehmele, F., Küpfer, K., Brand, J., Wisotzky, C., Skapski, J., Rentz, L., Mohr, S., and Kunz, M.: Hochwasser Mitteleuropa, Juli 2021 (Deutschland): 21. Juli 2021 – Bericht Nr. 1 „Nordrhein-Westfalen amp; Rheinland-Pfalz", Tech.rep., https://doi.org/10.5445/IR/1000135730, 2021.

Schättler, U., Doms, G., and Schraff, C.: A Description of the Nonhydrostatic Regional COSMO-Model Part VII: User's Guicd, Tech. rep.,DeutscherWetterdienst, P.O. Box 100465, 63004 Offenbach, Germany, 2016.

Skok, G. and Roberts, N.: Analysis of Fractions Skill Score properties for random precipitation fields and ECMWF forecasts, Quarterly Journal of the Royal Meteorological Society, 142, 2599–2610, https://doi.org/10.1002/qj.2849, 2016.

Sørland, S. L., Brogli, R., Pothapakula, P. K., Russo, E., Van de Walle, J., Ahrens, B., Anders, I., Bucchignani, E., Davin, E. L., Demory, M.-E., Dosio, A., Feldmann, H., Früh, B., Geyer, B., Keuler, K., Lee, D., Li, D., van Lipzig, N. P. M., Min, S.-K., Panitz, H.-J., Rockel, B., Schär, C., Steger, C., and Thiery, W.: COSMO-CLM regional climate simulations in the Coordinated Regional Climate Downscaling Experiment (CORDEX) framework: a review, Geosci. Model Dev., 14, 5125–5154, https://doi.org/10.5194/gmd-14-5125-2021, 2021.

Stucki, P., Rickli, R., Brönnimann, S., Martius, O., Wanner, H., Grebner, D., and Luterbacher, J.: Weather patterns and hydro-climatological precursors of extreme floods in Switzerland since 1868, Meteorologische Zeitschrift, 21, 531–550, https://doi.org/10.1127/0941-2948/2012/368, 2012.

Tiedtke, M.: A comprehensive mass flux scheme for cumulus parameterization in large-scale models, Mon. Weather Rev., 117, 1779–1800, https://doi.org/10.1175/1520-0493(1989)117<1779:ACMFSF>2.0.CO;2, 1989.

Toreti, A., Xoplaki, E., Maraun, D., Kuglitsch, F. G., Wanner, H., and Luterbacher, J.: Characterisation of extreme winter precipitation in Mediterranean coastal sites and associated anomalous atmospheric circulation patterns, Natural Hazards and Earth System Sciences, 10, 1037–1050, https://doi.org/10.5194/nhess-10-1037-2010, 2010.

1335 Tramblay, Y., Feki, H., Quintana-Seguí, P., and Guijarro, J. A.: The SAFRAN daily gridded precipitation product in Tunisia (1979–2015), International Journal of Climatology, 39, 5830–5838, https://doi.org/10.1002/joc.6181, 2019.

Ulbrich, U., Christoph, M., Pinto, J. G., and Corte-Real, J.: Dependence of Winter Precipitation Over Portugal on NAO and Baroclinic Wave Activity, International Journal of Climatology, 19, 379–290, 1999.

Uppala, S. M., KÅllberg, P. W., Simmons, A. J., Andrae, U., Bechtold, V. D. C., Fiorino, M., Gibson, J. K., Haseler, J.,
1340   Hernandez, A., Kelly, G. A., Li, X., Onogi, K., Saarinen, S., Sokka, N., Allan, R. P., Andersson, E., Arpe, K., Balmaseda, M. A., Beljaars, A. C. M., Berg, L. V. D., Bidlot, J., Bormann, N., Caires, S., Chevallier, F., Dethof, A., Dragosavac, M., Fisher, M., Fuentes, M., Hagemann, S., Hólm, E., Hoskins, B. J., Isaksen, L., Janssen, P. A. E. M., Jenne, R., Mcnally, A. P., Mahfouf, J.-F., Morcrette, J.-J., Rayner, N. A., Saunders, R. W., Simon, P., Sterl, A., Trenberth, K. E., Untch, A., Vasiljevic, D., Viterbo, P., and Woollen, J.: The ERA-40 re-analysis, Quarterly Journal
1345   of the Royal Meteorological Society, 131, 2961–3012, https://doi.org/10.1256/qj.04.176, 2005.

Vanden-Broucke, S., Wouters, H., Demuzere, M., and van Lipzig, N. P. M.: The influence of convection-permitting regional climate modeling on future projections of extreme precipitation: dependency on topography and timescale, Climate Dynamics, 52, 5303–5324, https://doi.org/10.1007/s00382-018-4454-2, 2018.

Werner, P. and Gerstengarbe, F.-W.: Catalog of the general weather situations of Europe, Potsdam Institute for Climate Impact
1350   Research (PIK) , https://www.pik-potsdam.de/en/output/publications/pikreports/.files/pr119.pdf, [online; accessed 10 Nov 2022], 2010.

Xiang, Y., Chen, J., Li, L., Peng, T., and Yin, Z.: Evaluation of Eight Global Precipitation Datasets in Hydrological Modeling, Remote Sensing, 13, 2831, 2021.

Yang, J., Duan, S.-B., Zhang, X., Wu, P., Huang, C., Leng, P., and Gao, M.: Evaluation of Seven Atmospheric Profiles from
1355   Reanalysis and Satellite-Derived Products: Implication for Single-Channel Land Surface Temperature Retrieval, Remote Sensing, 12, 791, https://doi.org/10.3390/rs12050791, 2020.